

Enhanced Multiphase Circumgalactic Medium and Gas Cycling in Galaxy Mergers

MAOLAN YANG ^{1,2} SUOQING JI ^{3,4} ROBERT FELDMANN ⁵ FENG YUAN ³ JORGE MORENO ⁶ TAOTAO FANG ⁷
CORAL WHEELER ⁸ LUIGI BASSINI ⁹ JING WANG ¹⁰ JONATHAN STERN ¹¹ CLAUDE-ANDRÉ FAUCHER-GIGUÈRE ¹² AND
DUŠAN KEREŠ ¹³

¹Shanghai Astronomical Observatory, Chinese Academy of Sciences, Shanghai 200030, P.R.China

²University of Chinese Academy of Sciences, 19A Yuquan Road, Beijing 100049, P.R.China

³Center for Astronomy and Astrophysics and Department of Physics, Fudan University, Shanghai 200438, P.R.China; sqji@fudan.edu.cn; fyuan@fudan.edu.cn

⁴Key Laboratory of Nuclear Physics and Ion-Beam Application (MOE), Fudan University, Shanghai 200433, P.R.China

⁵Department of Astrophysics, University of Zurich, Zurich CH-8057, Switzerland; robert.feldmann@uzh.ch

⁶Department of Physics and Astronomy, Pomona College, Claremont, CA 91711, USA

⁷Department of Astronomy, Xiamen University, Xiamen, Fujian 361005, People's Republic of China

⁸Department of Physics and Astronomy, California State Polytechnic University, Pomona, Pomona, CA 91768, USA

⁹Department of Astrophysics, University of Zurich, Winterthurerstrasse 190, Zurich CH-8057, Switzerland

¹⁰Kavli Institute for Astronomy and Astrophysics, Peking University, Beijing 100871, People's Republic of China

¹¹School of Physics and Astronomy, Tel Aviv University, Tel Aviv 69978, Israel

¹²CIERA and Department of Physics and Astronomy, Northwestern University, 1800 Sherman Ave, Evanston, IL 60201, USA

¹³Center for Astrophysics and Space Sciences, University of California San Diego, San Diego, CA 92093, USA

(Dated:)

ABSTRACT

We investigate the impact of galaxy mergers on the circumgalactic medium (CGM) using the FIREbox cosmological hydrodynamic simulation. By comparing matched samples of merging and isolated galaxies with stellar masses $M_{\star} \sim 10^{10} - 10^{11} M_{\odot}$ at $z = 0$ and mass ratio of merging galaxies larger than 1 : 10, we find that mergers significantly alter CGM properties. Merging systems exhibit enhanced radiative cooling, leading to shorter cooling times than free-fall times across large CGM volumes. This results in amplified multiphase structure and increased cool/cold gas content ($T \sim 10^4$ K) compared to isolated galaxies. Both inflow and outflow mass fluxes are elevated by at least ~ 1 dex in mergers across all temperature phases, with cool gas primarily generated in-situ via radiative cooling rather than from pre-existing streams. Gas cycling analysis reveals that mergers fundamentally accelerate CGM processing, amplifying the effective transfer rate from cold/cool cosmic inflow to galaxy inflow by factors of ~ 30 , through rapid cycling of inflowing gas through intermediate CGM phases, efficiently fueling the ISM and star formation. The enhanced cool gas content in mergers produces elevated column densities for low- and intermediate-temperature ion species in the inner CGM, while high-temperature ones remain largely unaffected.

Keywords: Galaxy evolution (594) — Interacting galaxies (802) — Circumgalactic medium (1879) — Hydrodynamical simulations (767)

1. INTRODUCTION

The circumgalactic medium (CGM) is a crucial component in galaxy formation and evolution. Although its strict definition is not universally agreed upon in the community, the CGM is generally considered to be the gas residing in the region between the edge of a galaxy and the virial radius of its host halo. In most L^{\star} galaxies, the CGM is thought to be dominated by hot, diffuse gas with a temperature of $\sim 10^6$ K (G. Münch & H. Zirin 1961; J. N. Bahcall & L. Spitzer 1969), while numerous observations reveal the widespread presence

of cooler components, leading to a multiphase CGM scenario (J. Tumlinson et al. 2017; J. X. Prochaska et al. 2017a; F. S. Zahedy et al. 2019; J. K. Werk et al. 2013; G. Zhu & B. Ménard 2013; Z. Qu et al. 2022). The properties of the CGM are shaped by both various large-scale processes and multiple small-scale physics (C.-A. Faucher-Giguère & S. P. Oh 2023). The former one includes the baryon cycle (R. J. Wright et al. 2024; D. Anglés-Alcázar et al. 2017; M. Donahue & G. M. Voit 2022) that gas is accreted from the intergalactic medium and flows out from galaxies via stellar feedback and AGN

feedback, and virial heating by the gravitational potential of the host halo (J. Stern et al. 2020). These are further regulated by various physical mechanisms in small-scale such as radiative cooling (M. McCourt et al. 2012; G. M. Voit et al. 2017; M. Gronke & S. P. Oh 2018), turbulence mixing layers (S. Ji et al. 2019; D. B. Fielding et al. 2020; B. Tan & S. P. Oh 2021), magnetic fields (S. Ji et al. 2018; M. Gronke & S. P. Oh 2020; D. Nelson et al. 2020; F. van de Voort et al. 2021), and cosmic rays (S. Ji et al. 2020; M. Ruszkowski et al. 2017; P. F. Hopkins et al. 2020; S. Ji et al. 2021). Due to the large amount of baryons contained in the CGM, it plays a significant role in galaxy formation and evolution by acting as a reservoir of gas and a conduit connecting galaxies to their surrounding environment, thereby regulating the star formation process within galaxies.

Galaxy mergers have been extensively studied from both observational and theoretical perspectives. Observationally, mergers are believed to play a key role in triggering star formation (S. L. Ellison et al. 2008; D. R. Patton et al. 2013; Q. Huang et al. 2025), galaxy quenching (S. L. Ellison et al. 2022), active galactic nucleus (AGN) activity (S. L. Ellison et al. 2011; X. Liu et al. 2011; G. Jin et al. 2021), and affecting the interstellar medium (ISM) by, e.g., decreasing metallicity and supplying cold gas (S. L. Ellison et al. 2008). Theoretically, the violent perturbations of the gravitational potential and the transfer of angular momentum during mergers are thought to drive these phenomena. Modern numerical simulations, both idealized and cosmological, now allow us to investigate the detailed physical processes occurring during mergers and to study the properties of the galaxies involved with greater sophistication (e. g. J. Moreno et al. 2015; J. Moreno et al. 2019; D. R. Patton et al. 2020; J. Moreno et al. 2021; M. Sparre et al. 2022; Y. Deng et al. 2025).

In particular, modern cosmological simulations and zoom in simulations provide a powerful tool to study mergers in a realistic context, revealing the interplay between mergers and their environments. During a merger, gas inflows from the CGM are enhanced by the interaction between the two galaxies (M. Sparre et al. 2022), leading to increased star formation rates (D. R. Patton et al. 2020) and potentially triggering AGN activity (S. Quai et al. 2023). The CGM itself is also affected by the merger, which can store the expelled gas from the galaxy via tidal forces, stellar feedback and/or AGN feedback (M. H. Hani et al. 2018). These processes may shape the observed properties of the CGM, including its metal content, multiphase structure, spatial distribution, and kinematic state. Understanding this two-way interaction between mergers and the CGM is therefore crucial for a complete picture of how mergers drive galaxy evolution, yet the detailed physical mechanisms remain incompletely understood.

Despite significant progress in both simulations and observations, comprehensive studies of the CGM during merger

events remain limited. While pioneering simulation work has begun to explore CGM-merger connections (e.g., M. H. Hani et al. 2018; M. Sparre et al. 2022), most studies have employed idealized merger setups in isolation, which necessarily simplify the cosmological environment and the continuous baryon cycling between the intergalactic medium, CGM, and galaxies. Furthermore, the primary focus has typically been on galactic properties such as star formation and ISM kinematics (J. Moreno et al. 2019; D. R. Patton et al. 2020; J. Moreno et al. 2021), with the CGM often characterized through integrated properties rather than a detailed examination of its multiphase structure, spatial evolution, and the interplay of multiple physical processes (e.g., cooling, mixing, feedback) acting simultaneously. Observationally, while absorption line and radio emission studies have revealed rich CGM structures around galaxies (J. Tumlinson et al. 2017; J. X. Prochaska et al. 2017a; J. Wang et al. 2023), systematically connecting these observations to merger-driven processes remains challenging. Consequently, key questions regarding the response of the multiphase CGM to mergers and the underlying physical mechanisms persist, addressing which requires simulations that combine cosmological environments with CGM multiphase structure and track the relevant physical processes.

In this work, we address these questions by conducting a systematic study of the CGM during galaxy mergers within a fully cosmological framework. We utilize the modern hydrodynamic cosmological simulation FIREbox (R. Feldmann et al. 2023), which is based on the FIRE-2 physics model¹⁴ (P. F. Hopkins et al. 2018) and combines a large cosmological volume with the key physical processes governing the evolution of the multiphase CGM. This allows us to investigate mergers in their proper cosmological context while resolving the detailed interplay between mergers and the multiphase CGM. As an illustration, Fig. 1 shows two merging galaxies alongside an isolated control galaxy from FIREbox at $z = 0$. The merging system on the leftmost column hosts three galaxies with stellar masses of $2.2 \times 10^{10} M_{\odot}$, $8.4 \times 10^9 M_{\odot}$ and $8.0 \times 10^9 M_{\odot}$, the center one has total stellar mass of $2.1 \times 10^{10} M_{\odot}$, while the rightmost isolated galaxy have stellar mass of $4.1 \times 10^{10} M_{\odot}$. The merging galaxies exhibit notably more disturbed CGM structures compared to the isolated galaxy, with a higher prevalence of cool gas and increased inflow velocities. The starburst merger, in particular, displays pronounced outflow velocities driven by intense stellar feedback triggered by the interaction. We detail our methods and present comprehensive results in the following sections.

The paper is organized as follows. In §2, we describe the numerical simulations with the physics included in our study.

¹⁴ <http://fire.northwestern.edu>

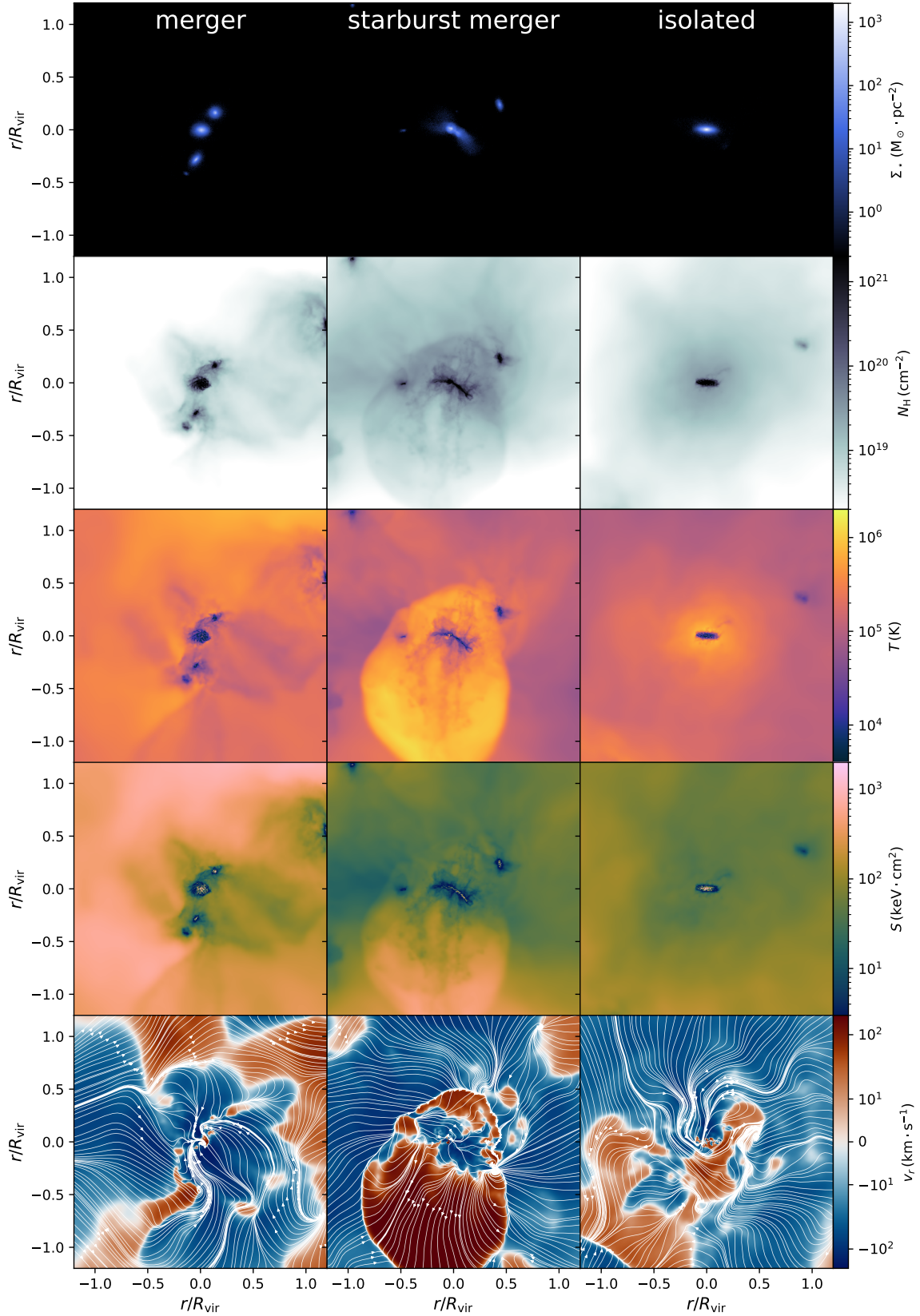


Figure 1. Projected distributions of key physical properties across three galactic systems. From top to bottom: stellar surface density, gas density, gas density-weighted temperature, entropy, and radial velocity. The panels show a typical galaxy merger hosting three galaxies with stellar masses of $2.2 \times 10^{10} M_{\odot}$, $8.4 \times 10^9 M_{\odot}$ and $8.0 \times 10^9 M_{\odot}$ (left column), a starburst merger with stellar mass of $2.1 \times 10^{10} M_{\odot}$ (middle column), and a corresponding isolated control galaxy with stellar mass of $4.1 \times 10^{10} M_{\odot}$ (right column) at $z = 0$. The merger systems exhibit more disturbed CGM structures than the isolated galaxy, with more cool gas and higher inflow velocities. The starburst merger shows particularly strong outflow velocities due to intense stellar feedback triggered by the interaction.

In §3, we show the results of our simulations. We finally discuss the implications of our results and conclude in §4.

2. METHODS

2.1. An overview of the FIREbox simulation

This study utilizes the FIREbox cosmological hydrodynamic simulation (R. Feldmann et al. 2023), which implements the FIRE-2 physics framework (P. F. Hopkins et al. 2018) using the meshless finite-mass methodology incorporated in the GIZMO code (P. F. Hopkins 2015). The FIREbox simulation suite models the co-evolution of gas, stellar populations, and dark matter within a periodic cosmological volume of $(15 \text{ Mpc}/h)^3$. Our analysis employs the highest-resolution simulation from this suite, designated “FB1024” in R. Feldmann et al. (2023), which incorporates 1024^3 gas particles and 1024^3 dark matter particles. This configuration achieves a mass resolution of $m_b = 6.26 \times 10^4 M_\odot$ for baryonic matter and $m_{\text{DM}} = 3.35 \times 10^5 M_\odot$ for dark matter. The simulation adopts cosmological parameters consistent with Planck Collaboration measurements (Planck Collaboration et al. 2016): $h = 0.6774$, $\Omega_m = 0.3089$, $\Omega_\Lambda = 0.6911$, $\Omega_b = 0.0486$, $\sigma_8 = 0.8159$, and $n_s = 0.9667$. Initial conditions were generated at redshift $z = 120$ using the MUSIC (Multi-Scale Initial Conditions) code (O. Hahn & T. Abel 2011).

FIREbox incorporates the comprehensive FIRE-2 physics model, which accounts for critical baryonic processes including radiative cooling, heating mechanisms, star formation, and stellar feedback. The thermal evolution of gas spans a wide temperature range from 10 K to 10^{10} K, with cooling and heating calculations that incorporate free-free, photoionization, recombination, Compton, photoelectric, and dust-coupling processes. The simulation accounts for both local radiation sources and the metagalactic ultraviolet background as characterized by C.-A. Faucher-Giguère et al. (2009). Star formation occurs exclusively in gas that simultaneously satisfies multiple physical criteria: self-gravitating conditions, number densities exceeding 300 cm^{-3} , Jeans instability, and molecular (self-shielding) state. Stellar feedback is implemented through multiple channels, including Type Ia and Type II supernovae that inject mass, momentum, energy, and metals into the surrounding medium, as well as mass loss from OB and AGB stars via stellar winds. Additionally, the simulation incorporates radiative feedback mechanisms from these stellar populations. It should be noted that the FIREbox simulation we analyze in this paper does not include active galactic nucleus (AGN) feedback or cosmic ray physics.

2.2. Sample galaxy selection

To investigate the effects of galaxy mergers on CGM properties, we constructed statistically meaningful samples of both merging and isolated galaxies from the FIREbox simulation

at $z = 0$. Our selection procedure followed a hierarchical approach, beginning with host halo identification and concluding with matched merger-control galaxy pairs.

First, we utilized the halo catalogs generated by AHF (S. P. D. Gill et al. 2004; S. R. Knollmann & A. Knebe 2009) to identify suitable host halos within the FIREbox data. We established a lower central galaxy baryon mass threshold of $10^{10} M_\odot$, which guarantees that the CGM in our sample halos is resolved by at least $\sim 10^5$ particles for the given baryon mass resolution, providing adequate sampling of CGM structure and multiphase properties. Some galaxies are hosted by halos that reside within the virial radius of a more massive halo (usually called subhalo), and thus the CGM may be influenced by the more massive halo and to distinguish contribution sophisticatedly from the central galaxy and the more massive galaxy is difficult. To avoid this complication, we excluded all halos identified as subhalos by AHF. After applying these criteria, we identified 70 host halos at $z = 0$ suitable for further analysis.

Within these selected halos, we then classify galaxies as either merging or isolated based on their interaction history. We define a galaxy as a merging galaxy if it is either currently undergoing a merger or has experienced a merging event within the past 1 Gyr; otherwise, it was classified as isolated. Due to the small number of host halos resulted from the last procedure, we simply distinguish whether a galaxy is a merging galaxy through visual classification. We also imply a mass ratio threshold of 1 : 10 to all alternative merger samples to avoid possible bias. We chose the 1 Gyr threshold to capture the timescale over which merger-induced perturbations can propagate through and relax within the CGM. We define this minimum relaxation interval as the maximum of some characteristic timescale governing CGM response to mergers. Among the physically motivated estimates for the relaxation timescale is provided by the sound-crossing time, $t_{\text{sc}} \sim R/c_s$, where R is a characteristic CGM scale and c_s is the sound speed. Adopting $R \sim R_{\text{vir}} \propto M_{\text{halo}}^{1/3} (1+z)^{-1}$ and $c_s \propto T_{\text{CGM}}^{1/2}$, this yields the scaling

$$t_{\text{sc}} \sim 0.6 \text{ Gyr} \left(\frac{M_h}{10^{11} M_\odot} \right)^{1/3} \left(\frac{T_{\text{CGM}}}{10^6 \text{ K}} \right)^{-1/2} \left(\frac{1+z}{1} \right)^{-1}. \quad (1)$$

If the CGM temperature tracks the virial temperature, $T_{\text{CGM}} \sim T_{\text{vir}} \propto M_{\text{halo}}^{2/3} (1+z)$, the mass dependence largely cancels, yielding characteristic sound-crossing times of order 1 Gyr at $z \sim 0$ for our sample, justifying our choice of merger timescale. Additional relevant timescales include the dynamical time and the cooling time of the CGM, but these are generally comparable to or shorter than the sound-crossing time for our sample. This threshold is somewhat shorter than merger definitions adopted in some observational studies (e.g., M. H. Hani et al. 2020), but is well-suited for cap-

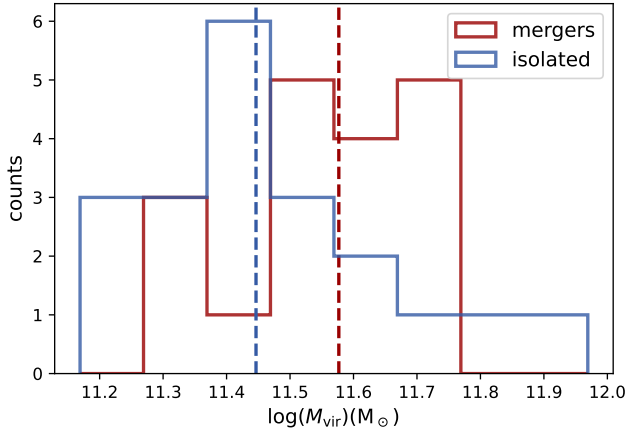


Figure 2. Virial mass distributions of host halos, showing the counts of halos hosting merging galaxies (red histogram) and halos hosting isolated galaxies (blue histogram) within given virial mass bins. The red (blue) dashed vertical lines indicate the median virial masses of merging (isolated) galaxy host halos. Virial masses of selected halos range from $10^{11} M_{\odot}$ to $10^{12} M_{\odot}$.

turing merger-induced CGM perturbations in our simulation analysis.

For each identified merging galaxy, we construct control samples from the isolated galaxy population by matching gas and stellar mass properties. An isolated galaxy is selected as a control if it exhibits similar gas and stellar mass to a merging galaxy. Each merger is required to have at least one matching control galaxy to be included in our final sample. For mergers with multiple potential controls, we selected up to three isolate galaxies with the closest matching gas and stellar mass. To maximize statistical power, we allow individual isolated galaxies to serve as controls for multiple mergers when appropriate. This matching procedure yields a final sample of 18 merging galaxies paired with 20 control galaxies and 44 merger-control pairs for comparative analysis. There are 11 major mergers with mass ratio larger than 1 : 3 and 7 minor mergers with mass ratio lower than 1 : 3 inside our merging galaxies sample.

2.3. Properties of the selected galaxy sample

Fig. 2 presents the virial mass distributions of host halos for both merging (red histogram) and control (blue histogram) galaxies. The vertical dashed lines indicate the median virial masses for each population. Merging galaxies preferentially reside in slightly more massive halos than isolated systems, though the two distributions substantially overlap, indicating that halo mass alone does not strongly discriminate between the two populations. Fig. 3 shows the stellar and gas mass distributions of primary and secondary galaxies in our merger sample, displayed as blue dots and red squares, respectively. Secondary stellar and gas masses broadly correlate with primary stellar mass, as expected for mass-selected pairs, though

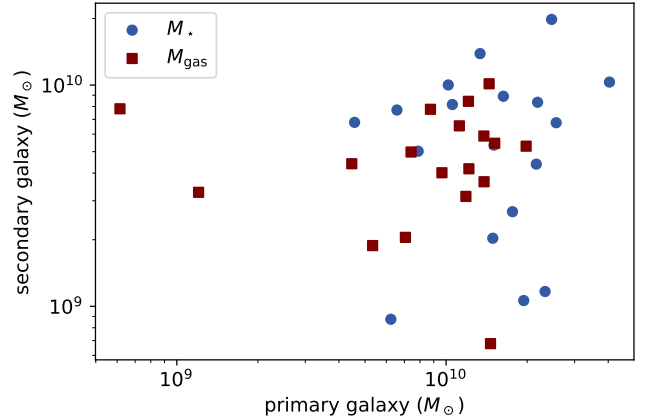
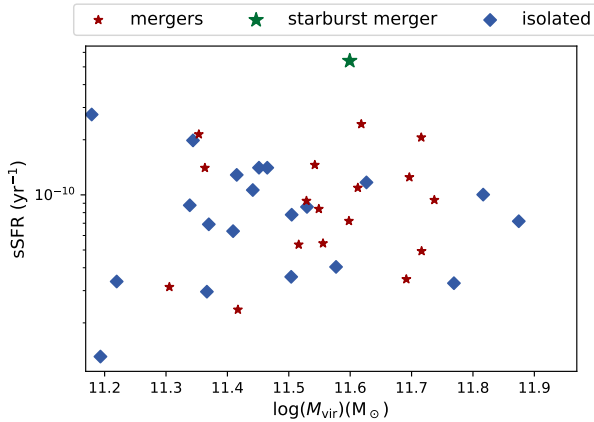


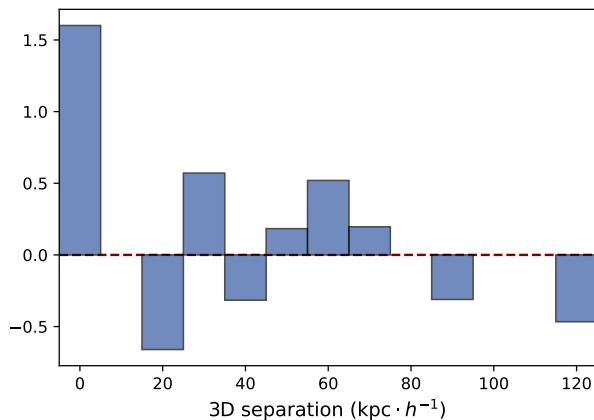
Figure 3. Stellar mass and gas mass distribution of the primary galaxies and secondary galaxies in merging pairs (blue dots and red squares, respectively). Our sample covers a stellar mass range of $3 \times 10^9 M_{\odot}$ to $4 \times 10^{10} M_{\odot}$, and a gas mass range of $5 \times 10^8 M_{\odot}$ to $2 \times 10^{10} M_{\odot}$.

gas masses exhibit larger scatter at fixed stellar mass. Most galaxies in our sample are dwarf or sub- L^* systems with stellar masses ranging from $3 \times 10^9 M_{\odot}$ to $4 \times 10^{10} M_{\odot}$, gas masses between $5 \times 10^8 M_{\odot}$ and $2 \times 10^{10} M_{\odot}$, and host halo virial masses below $10^{11.9} M_{\odot}$. This predominance of lower-mass systems results from both the limited volume of the FIREbox simulation and our selection criteria. While FIREbox reproduces the theoretical halo mass function within 0.2 dex (see R. Feldmann et al. 2023, Appendix A), the scarcity of halos with virial masses exceeding $10^{12} M_{\odot}$ is a direct consequence of the simulation’s finite volume. Additionally, our exclusion of galaxies with numerous satellites eliminates many massive halos, further limiting the available massive systems for constructing control samples.

Fig. 4a displays the specific star formation rates (sSFRs) of merging and isolated galaxies as a function of host halo virial mass. Merging galaxies typically exhibit sSFR values comparable to isolated systems, with most values near 10^{-10} yr^{-1} , consistent with the star-formation main sequence. To quantify merger-induced star formation enhancement, we define the sSFR enhancement as the ratio $\text{sSFR}_{\text{merger}} / \text{mean}(\text{sSFR}_{\text{isolated}})$ and plot it as a function of three-dimensional pair separation in Fig. 4b, where coalesced systems are assigned a separation of 0 kpc and the red dashed line denotes no enhancement (ratio = 1). We find that 10 out of 18 mergers exhibit sSFR enhancement, in agreement with previous observational and simulation studies (e.g., S. L. Ellison et al. 2008; D. R. Patton et al. 2013; J. Moreno et al. 2015; J. Moreno et al. 2019; J. Moreno et al. 2021). The enhancement tends to be strongest near coalescence, though with substantial scatter. One merging pair stands out as undergoing a merger-triggered starburst phase, with $\text{sSFR} \gtrsim 5 \times 10^{-9} \text{ yr}^{-1}$,



(a) sSFR vs. virial mass



(b) sSFR enhancement

Figure 4. Fig. 4a: Specific star formation rate of merging galaxies and control galaxies versus virial masses of host halos at $z = 0$. Merging galaxies are indicated with stars while control galaxies are indicated with blue octagons. A notable merging pair with high sSFR is marked in green and labeled as “starburst merger,” while other merging samples are marked in red. Fig. 4b: Enhancement of specific star formation rate (sSFR), defined as $\text{sSFR}_{\text{merger}}/\text{mean}(\text{sSFR}_{\text{isolated}})$, for merging galaxies relative to the mean sSFR of isolated galaxies, plotted as a function of the separation between merging galaxies; systems that have coalesced are assigned a separation of 0. The red dashed line indicates no enhancement (ratio = 1).

approximately half an order of magnitude above the sample median. We refer to this system as the “starburst merger” in subsequent analyses and highlight it in green in Fig. 4a.

2.4. Defining the CGM

To isolate the CGM from galactic ISM, we exclude all galactic regions (including the central galaxy, merging galaxies, and any satellite galaxies) from consideration. We identify galaxies by applying a friends-of-friends algorithm to stellar particles with a ~ 1.5 kpc (or $1 \text{ kpc}/h$ which equals one code length at $z = 0$ in FIREbox simulation) linking length (V.

Springel et al. 2001). Only stellar aggregations exceeding $10^{-3} M_{\star, \text{tot}}$ of the halo’s total stellar mass are classified as galaxies. Each galaxy’s region is defined as a sphere centered on its mass-weighted center with radius twice the distance from the center to the farthest stellar particle. We checked this radius selection method for every galaxy and found it didn’t suffer from extreme situations like stellar particles that are very far away and could result in galaxy radius that separates the galaxy and CGM well. We also tested other radius definitions, such as the radius of 99th-farthest stellar particle or the half mass radius. While in some cases (for example, in isolated galaxies) these definition works well and give consistent results with the method we adopt, they may generate too large or too small radii in some other galaxies especially in merging ones, which may be the result of the sparse stellar distribution due to tidal effect. In this manner we identify all galaxies within each host halo and treat gas inside these galactic spheres as ISM. The outer boundary of the CGM is somewhat arbitrary; a common convention is to define the CGM as the gaseous halo within the virial radius (e.g., J. Tumlinson et al. 2017; Z. Hafen et al. 2019; M. Sparre et al. 2020). In this work, we therefore define the CGM as all gas within the host halo’s virial radius but outside any galactic spheres. This method yields galaxy radii of 15–55 kpc with a median radius of 21 kpc, or galaxy-to-virial-radius ratios of 0.08–0.30 with a median of 0.11 for the central galaxies in our sample.

The method we use to define the CGM is not exactly the same as that used in some previous studies (e.g., M. Sparre et al. 2020; J. Stern et al. 2021). Some studies utilize several halos and use a fix ratio to R_{vir} to define the inner boundary of the CGM, which is suitable for their specific scientific goals. However, we find some limitations of this approach in our case, including, for example, some galaxies having very extended and sparse stellar distributions, some halos hosting multiple galaxies with large mass differences, and large scale stellar tidal structures in some merging systems. These factors can lead to contamination of CGM measurements by ISM gas if a fixed fraction of R_{vir} is used as the inner CGM boundary. Some studies use similar methods to ours to define the CGM (Z. Hafen et al. 2019), while the specific details such as the way to identify galaxies may vary. Even though, we note that these different CGM definitions—including ours—lead to similar CGM inner boundaries in most cases and thus should not significantly affect our main results.

2.5. Scatter calculation

Because the CGM distribution is asymmetric (see Fig. 1), a single radial profile without uncertainty does not fully reveal the distribution of CGM in galaxies and capture differences between merging and isolated galaxies; while a single median line can hide substantial galaxy-to-galaxy and intra-galaxy

variation. For each galaxy we therefore compute the radial distribution of values at each radius and derive that galaxy’s mean radial profile and per-radius distribution. To obtain a representative profile for each population, we take the median of the galaxies’ mean profiles separately for merging and isolated samples. We use a bootstrapping method to estimate uncertainties in the median profiles. To illustrate the full spread, we combine the per-radius distributions across all galaxies in the same population and display the 16th–84th percentile range as a shaded band in the figures. For the starburst merger (the sole member of its category) the plotted profile reduces to its individual profile and the shaded band to its own 16th–84th percentile range.

We apply an analogous procedure when computing mass and metal fluxes through spherical shells (Fig. 7): we compute the flux through each shell for every galaxy, then present the median flux at each radius for the merging and isolated populations. At a given radius each galaxy contributes a single flux value; the scatter is thus the 16th–84th percentile range across galaxies in the population. No scatter is shown for the single starburst merger.

3. RESULTS

3.1. Spatial properties

Figure 1 illustrates the distinct representative CGM morphologies across different galactic environments. We select one typical galaxy merger that includes three galaxies with stellar masses of $2.2 \times 10^{10} M_{\odot}$, $8.4 \times 10^9 M_{\odot}$ and $8.0 \times 10^9 M_{\odot}$, the starburst merger highlighted in Fig. 4a with total stellar mass of $2.1 \times 10^{10} M_{\odot}$ (as the two galaxies are strongly merging, it’s difficult to identify their masses respectively) and an isolated control galaxy with stellar mass of $4.1 \times 10^{10} M_{\odot}$ to show this difference.

The typical galaxy merger (left column) exhibits a triple galaxies system clearly visible in the stellar surface density panel, with three distinct galactic structures in various stages of interaction. This system displays asymmetric gas distributions with pronounced tidal features and enhanced gas density in the bridge regions connecting the interacting galaxies. The temperature distribution reveals significant cool gas concentrations along these interaction interfaces, accompanied by low-entropy regions indicative of enhanced radiative cooling. The velocity structure demonstrates complex patterns comprising both inflows toward the galactic centers and non-equilibrium motions in the extended halo.

The starburst merger (middle column) presents two galaxies in direct collision, as shown in the stellar surface density panel, creating more extreme conditions characterized by powerful bipolar outflows evident in the temperature, entropy, and radial velocity maps, with material being expelled at velocities exceeding 200 km s^{-1} . These outflows correspond to regions of elevated entropy, signifying thermal energy depo-

sition from vigorous stellar feedback processes triggered by the galactic collision.

In contrast, the isolated control galaxy (left column) displays a more regular, quasi-spherical distribution across all properties, exhibiting a smooth temperature gradient and ordered infall pattern characteristic of a virialized halo in hydrostatic equilibrium. Although the velocity panel shows some inhomogeneity, the magnitude is less than it in the mergers. The entropy structure in merging systems reveals substantial mixing between different gas phases, disrupting the stratification evident in the isolated case. These visualizations illustrate how galaxy interactions fundamentally alter the thermodynamic and kinematic properties of the CGM, creating conditions conducive to enhanced gas cooling and accretion, as quantified in subsequent analyses.

3.2. CGM gas phases

While the previous figure illustrates specific examples of different galactic systems, here we present the statistical analysis of CGM properties across our entire sample of merging and isolated galaxies at $z = 0$. Fig. 5 displays the radial profiles of CGM hydrogen number density ($n_{\text{H,CGM}}$) and temperature for both populations. We note that regions identified as galaxies (as defined in § 2.4) are excluded from these measurements to focus exclusively on circumgalactic material. For individual galaxies, we first compute mean radial profiles, then take the median value across each category to represent the characteristic profile of merging and isolated populations as described in § 2.5.

In both merging and isolated systems, $n_{\text{H,CGM}}$ exhibits a characteristic decline with increasing galactocentric distance, decreasing approximately exponentially from $\sim 10^{-3} \text{ cm}^{-3}$ in the inner halo to $\sim 10^{-5} \text{ cm}^{-3}$ near the virial radius, which is similar to previous works (e. g. L. Blitz & T. Robishaw 2000; R. Feldmann et al. 2013; Z. Hafen et al. 2019). Concurrently, the temperature profile remains relatively stable at a few 10^5 K throughout most of the halo, consistent with the expected virial temperature of the host dark matter halos. Merging galaxies display marginally higher $n_{\text{H,CGM}}$ in the outer CGM regions and slightly reduced temperatures in the inner CGM compared to their isolated counterparts, though these differences remain modest. This similarity in overall baryon content establishes an appropriate baseline for our subsequent comparative analyses, ensuring that observed differences in other properties are attributable to the merger state rather than disparities in total gas mass. The starburst merger exhibits a slight overall enhancement in both $n_{\text{H,CGM}}$ and temperature relative to typical mergers, reflecting the impact of powerful supernova-driven outflows and their subsequent thermalization in the halo. The apparent truncation of profiles at small radii in this particular system results from the exclusion of

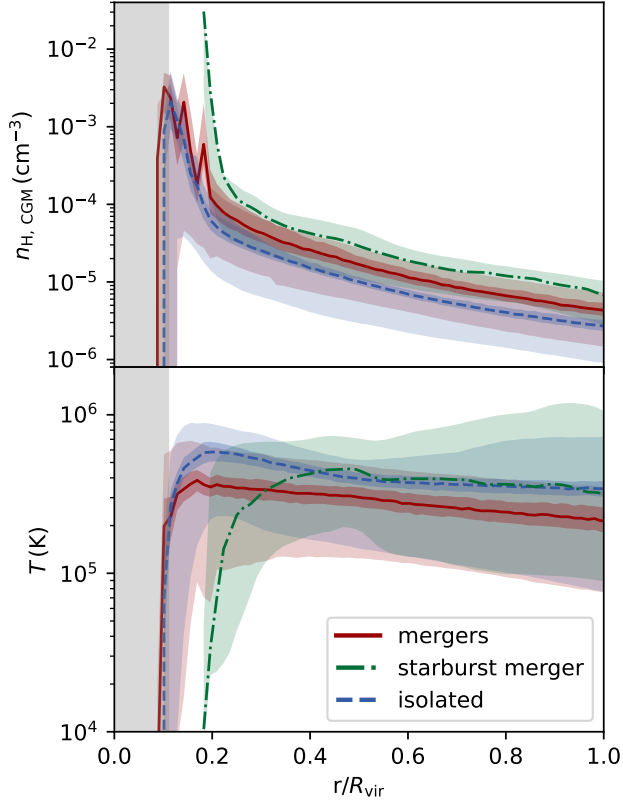


Figure 5. Radial profiles of hydrogen number density (top, volume-weighted) and temperature (bottom, density-weighted) for merging systems (red solid line), the starburst merger (green dash-dotted line), and isolated galaxies (blue dashed line), with galactocentric radius normalized to each halo’s virial radius R_{vir} . Profiles are sampled over all galaxies in each category at $z = 0$. Regions identified as galaxies are excluded from the analysis, while we use a gray band near $r/R_{\text{vir}} = 0$ to represent the median galaxy radius in our sample. Outer lighter shaded region colored with red, green and blue denote the 16th to 84th percentile ranges within each corresponding sample category. The inner darker shaded region around each line shows the 16th to 84th percentiles of the median value calculated via bootstrapping. Merging galaxies exhibit marginally higher gas densities in the outer CGM and slightly lower temperatures in the inner CGM compared to isolated systems. However, these differences remain relatively modest, confirming that our selected samples possess comparable halo baryon content.

overlapping galactic regions during the collision, where the distinction between individual galaxies becomes ambiguous.

Although the volume-weighted density and density-weighted temperature profiles of CGM gas in merging and isolated galaxies are broadly similar, indicating comparable total baryon content, mergers may nonetheless induce more substantial changes in the thermal structure of the CGM. To examine this, we present the density-weighted distribution of CGM gas in temperature- $n_{\text{H, CGM}}$ phase space in Fig. 6, sampled over all mergers (left panel), the starburst merger (middle panel), and isolated galaxies (right panel). The color

indicates the median probability density weighted by CGM gas mass for each sample. These phase diagrams are constructed by first calculating the probability density distribution of each galaxy’s CGM in temperature-density space, then taking the median value across all merging or isolated systems at each phase-space location. As most CGM gas is within $10^4 \text{ K} < T < 10^6 \text{ K}$, we take the same notations as in J. Tumlinson et al. (2017) to define cold gas ($T < 10^4 \text{ K}$), cool gas ($10^4 \text{ K} \leq T < 10^5 \text{ K}$), warm gas ($10^5 \text{ K} \leq T < 10^6 \text{ K}$) and hot gas ($T \geq 10^6 \text{ K}$). Although FIRE-2 models gas cooling down to $\sim 10 \text{ K}$ (P. F. Hopkins et al. 2018), it is less meaningful to discuss the explicit cold gas phase in CGM as the cold gas in CGM is rare in our samples.

Compared to isolated galaxies, merging systems exhibit a substantially broader distribution in phase space, particularly in the low-temperature, high-density regime characterized by temperatures of a few 10^4 K and $n_{\text{H, CGM}} \gtrsim 3 \times 10^{-4} \text{ cm}^{-3}$. This extended tail toward cooler, denser conditions indicates that mergers promote the formation of cool, dense gas in the CGM, consistent with the morphological features visible in Fig. 1. The starburst merger displays an even wider distribution in phase space, with significant populations of both cool, dense gas and hot, low-density gas—the latter resulting from vigorous stellar feedback during the intense starburst phase. There isn’t much gas with $T > 10^6 \text{ K}$ in either merging or isolated galaxies, as the halo mass scale considered here is $M_{\text{halo}} \sim 10^{11} M_{\odot}$, which will result a virial temperature of $\sim 10^5 \text{ K}$. In addition, the CGM is unlikely fully virialized in these halo with low halo mass as indicated in J. Stern et al. (2020).

3.3. Enhanced multiphase inflows and outflows

Galaxy merging events should not only impact the thermal properties of the CGM, but also the multiphase state of gas flows between the galaxies and the CGM. Here we examine how galaxy interactions affect the mass flux of CGM gas across different temperature phases. We show the cumulative mass flux integrated over $T < 10^5 \text{ K}$ and $T > 10^5 \text{ K}$ and differential mass flux distribution ($d\dot{M}/d \log T$) of CGM gas in Fig. 7. The mass flux is calculated at a radius of $R = 30 \text{ kpc}/h$ (or $\sim 0.25 R_{\text{vir}}$ in our samples), which is close enough to the galaxy region we defined in § 2.4 in most samples, while is not too small that enters the galaxy region in a large fraction of our samples as we identify different radius for different galaxy. We also test other radii near the galaxy and find that changing the specific value does not affect the result we show here except the specific quantities. Also, this radius selection is similar to other papers that study the inflow and outflow rates in CGM (e. g. A. L. Muratov et al. 2015; V. Pandya et al. 2021; L. Bassini et al. 2023), who adopt a radius around $0.25 R_{\text{vir}}$. We also use a similar method as in the papers mentioned above to calculate mass flux. In short, we

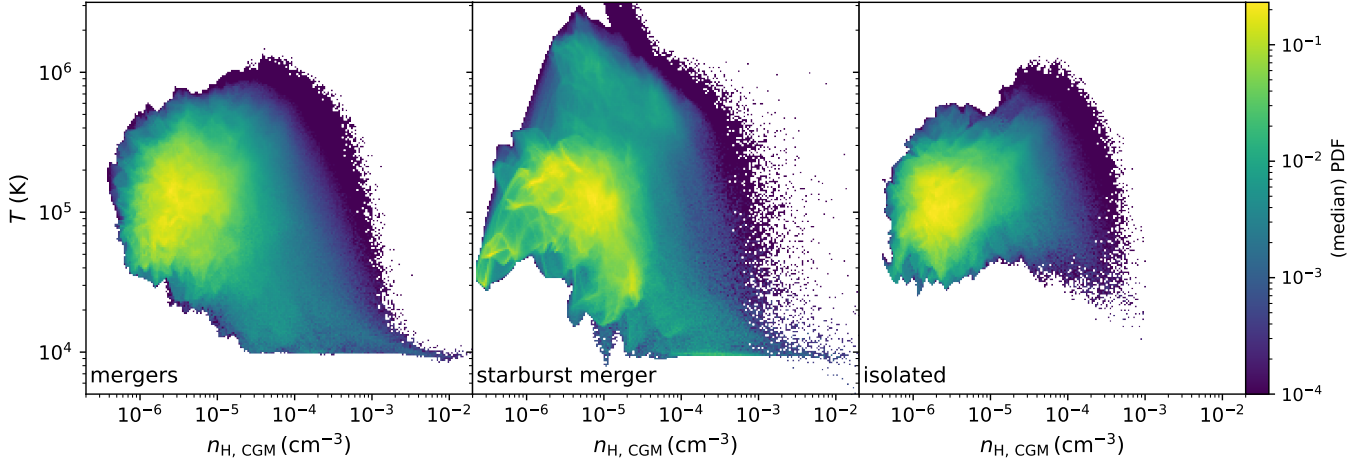


Figure 6. Density-weighted temperature- $n_{\text{H,CGM}}$ phase diagram of CGM gas in merging galaxies (left), starburst mergers (middle) and isolated galaxies (right). The phase diagram is sampled over all galaxies in each category at $z = 0$. Color indicates the median value of probability density weighted by CGM gas mass in merging or isolated galaxies. Gas with $T \sim 10^5$ K and $n_{\text{H,CGM}} \sim 10^{-6} \text{ cm}^{-3}$ dominates in both merging and isolated galaxies, but a wider distribution in phase space, especially in $10^4 \sim 10^5$ K, can be seen in mergers.

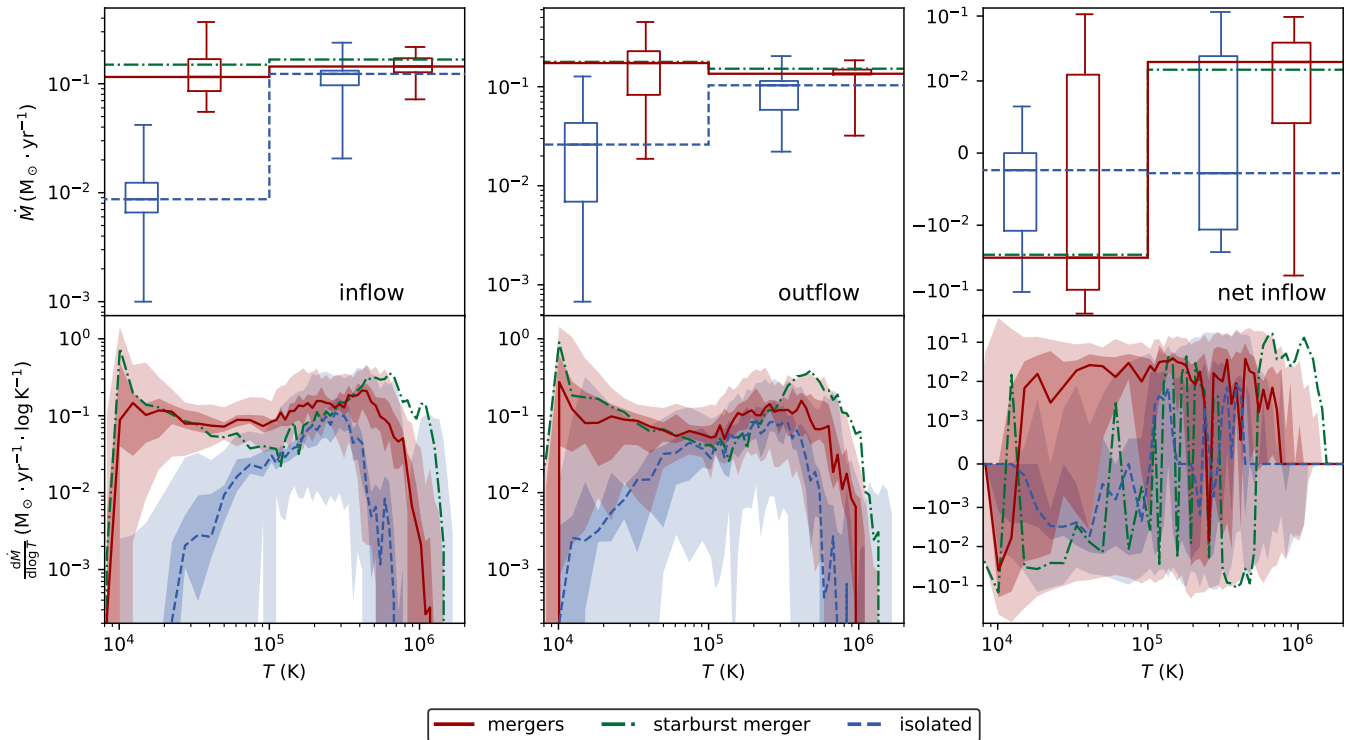


Figure 7. Mass flux of inflows (left), outflows (middle), and net inflows (right; positive values denote inflow) as a function of temperature at $R = 30 \text{ kpc}/h$, for merging galaxies (red solid), the starburst merger (green dash-dotted), and isolated control galaxies (blue dashed). *Top panels:* Cumulative mass flux integrated over $T < 10^5$ K and $T > 10^5$ K. Histograms show medians; boxes indicate the 16th–84th percentile range of the bootstrapped median; whiskers give the 16th–84th percentile range across the sample. *Bottom panels:* Differential mass-flux distribution, $dM/d \log T$. Curves denote medians; darker (lighter) shaded regions represent the 16th–84th percentile range of the bootstrapped median (full sample). Mergers exhibit systematically higher mass fluxes than isolated galaxies, particularly for cool gas ($T \lesssim 10^5$ K). The starburst merger shows comparable inflows but significantly enhanced outflows relative to typical mergers.

use a shell with radius between $25 \text{ kpc}/h$ and $35 \text{ kpc}/h$, and treat the particles falling into the halo (radial velocity $v_r < 0$) as inflow particles and the particles with $v_r > 0$ as outflow. Then we sum up the particles inside each temperature bin and normalize the sum with the temperature bin length and shell thickness. We show the cumulative mass flux in the tops panels where the histograms show the median value, boxes indicate the 16th to 84th percentile range of the median value calculated via bootstrapping, and whiskers give the 16th to 84th percentile range across the sample. The differential mass flux distribution is shown in the bottom panels where the curves denote the median value and the darker (lighter) shaded regions represent the 16th to 84th percentile range of the median value calculated via bootstrapping (full sample).

In isolated galaxies (blue), the median values of the inflow and outflow mass fluxes are both distributed over the temperature range $\sim 10^4 \text{ K}$ to $\sim 5 \times 10^6 \text{ K}$, with values from $\sim 10^{-3} M_\odot \text{ yr}^{-1} \log \text{ K}^{-1}$ at $T \sim 10^4 \text{ K}$ to $\sim 10^{-1} M_\odot \text{ yr}^{-1} \log \text{ K}^{-1}$ at $T \lesssim 10^6 \text{ K}$ for both inflow and outflow, and are negligible outside this range. As a result, the majority of inflow and outflow is the gas within 10^5 K to 10^6 K , contributing $\sim 0.13 M_\odot \text{ yr}^{-1}$ to the total median inflow rate and $\sim 0.13 M_\odot \text{ yr}^{-1}$ to the total median outflow rate, while the cool gas contributes only $\sim 0.007 M_\odot \text{ yr}^{-1}$ and $\sim 0.02 M_\odot \text{ yr}^{-1}$ respectively. Because the exchange rate is modest and almost balanced in isolated galaxies, the net mass flux is almost negligible, with little net outflow especially in $T > 10^5 \text{ K}$.

The situation is markedly different in merging galaxies (red). Both inflow and outflow mass fluxes are substantially enhanced across all temperatures, corresponding to roughly at least 1 dex increase in $T < 10^5 \text{ K}$ gas exchange and modest increase in $T > 10^5 \text{ K}$ gas relative to isolated galaxies. As a result, comparing with the situation in isolated galaxies, the inflow of cool and warm gas not only both increases to a median value of $\sim 0.11 M_\odot \text{ yr}^{-1}$ and $\sim 0.14 M_\odot \text{ yr}^{-1}$ but also becomes comparable. Outflow is also increased to the median value of $\sim 0.17 M_\odot \text{ yr}^{-1}$ and $\sim 0.13 M_\odot \text{ yr}^{-1}$ for cool gas and warm gas respectively. Moreover, the flux of $T \sim 10^4 \text{ K}$ gas is significantly boosted and even generates a remarkable peak. The net mass flux in merging galaxies is dominated by inflow and exhibits a plateau spanning from 10^4 K to $2 \times 10^5 \text{ K}$ for the majority of mergers. The net inflow of cool gas is affected by the high peak at $T \sim 10^4 \text{ K}$ of the outflow and becomes negative, but the scatter is large and most mergers show positive net inflow at higher temperatures as indicated in the lower panel. The net inflow of warm gas is changed to positive compared with isolated galaxies with a median value of $0.02 M_\odot \text{ yr}^{-1}$, implying a more efficient accretion in this phase during mergers.

For the starburst merger (green dash-dotted line), the behavior at $T \gtrsim 10^5 \text{ K}$ is similar to non-starburst mergers but with

stronger hot gas exchange due to intense stellar feedback, resulting a warm gas inflow and outflow rate of $\sim 0.17 M_\odot \text{ yr}^{-1}$ and $\sim 0.15 M_\odot \text{ yr}^{-1}$ respectively. However, the outflow at $T < 4 \times 10^4 \text{ K}$ is exceptionally strong and expels much of the cool gas from the galaxy. As a consequence, the inflow rate of cool gas is similar to non-starburst merger with a value of $\sim 0.15 M_\odot \text{ yr}^{-1}$, and the outflow rate increases to $\sim 0.18 M_\odot \text{ yr}^{-1}$, producing a net cool-gas outflow. The outflow strength at $T \sim 10^4 \text{ K}$ reaches the 84th percentile of the median value of our merging sample and is roughly one orders of magnitude higher than the median of other mergers at the peak.

In short, the multiphase nature of gas flows is significantly amplified in mergers: while isolated galaxies exhibit gas exchange concentrated within a relatively narrow temperature range, merging systems demonstrate simultaneous strong fluxes across a broad spectrum of temperatures from cool ($\sim 10^4 \text{ K}$) to hot ($\gtrsim 10^6 \text{ K}$) phases, reflecting a fundamentally more complex and dynamic multiphase CGM structure.

3.4. Merger-induced transition from hot-mode to cold-mode accretion

The enhanced cool gas inflows observed in merging galaxies can be attributed to more efficient radiative cooling in their CGM. To quantify this effect, we examine the ratio of cooling time to gravitational free-fall time, which is a key diagnostic of the dominant gas accretion mode. We compute the density-weighted cooling time $t_{\text{cool}} = 3kT/(2n\Lambda)$ as a function of galactocentric radius for the three categories, where Λ is the radiative cooling coefficients. For comparison, we calculate the gravitational free-fall time $t_{\text{ff}} = \sqrt{2r/|\nabla\Phi|}$, where Φ is the gravitational potential. Systems with $t_{\text{cool}} < t_{\text{ff}}$ are expected to exhibit cold-mode accretion, in which gas cools radiatively before falling onto the central galaxy, whereas those with $t_{\text{cool}} > t_{\text{ff}}$ experience hot-mode accretion, in which gas remains at elevated temperatures during infall and slowly cools near the galaxy after settling into the central regions. We present the results in Fig. 8.

In the isolated control galaxies, t_{cool} substantially exceeds t_{ff} throughout the CGM except in the inner region, consistent with a predominantly hot accretion mode in which inflowing gas remains at temperatures near the virial temperature and cools inefficiently. In contrast, merging systems including the starburst merger exhibit $t_{\text{cool}} < t_{\text{ff}}$ over significant portions of the CGM, extending to approximately half the virial radius, indicating a transition to cold-mode accretion wherein gas undergoes rapid radiative cooling before reaching the central galaxy. This condition is particularly pronounced in the starburst merger (green line), where $t_{\text{cool}} < t_{\text{ff}}$ holds nearly everywhere within the halo at $r \lesssim 0.8R_{\text{vir}}$. We note that the anomalously short cooling times observed in the outermost regions of the starburst merger ($r \gtrsim 0.8R_{\text{vir}}$) arise from the

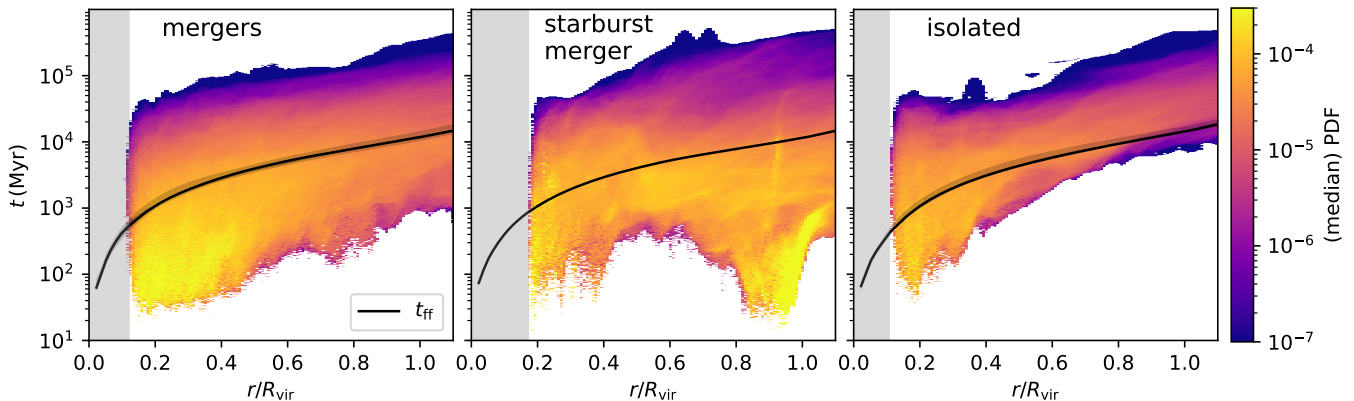


Figure 8. Radial profiles of the median density-weighted cooling time (the median value is acquired via the same method as in Fig. 6) in mergers (left), the starburst merger (middle), and the isolated galaxies (right), superposed with the median free-fall time (black solid line) and corresponding 16th to 84th percentile ranges of each category in light grey shaded regions. The 16th to 84th percentiles of the median free fall time is shown by deep grey shaded region which is, however, very close to the median value and thus almost invisible in the figure. In the isolated galaxies, t_{cool} generally exceeds t_{ff} throughout most of the halo except in the inner region, consistent with hot-mode accretion. In contrast, merging systems exhibit significant portions with $t_{\text{cool}} < t_{\text{ff}}$ especially in the CGM, indicating a transition to cold-mode accretion where radiative cooling operates efficiently. Note that the short cooling times in the outer regions ($r \gtrsim 0.8R_{\text{vir}}$) of the starburst merger reflect the accretion of warm, dense gas from the surrounding large-scale structure rather than merger-driven cooling within the established CGM.

presence of warm, high-density gas accreting from the surrounding large-scale structure and several galaxies near the edge of the halo rather than from merger-induced cooling processes within the established CGM itself.

These results demonstrate that galaxy interactions significantly alter the thermal structure of the CGM, triggering a transition from hot-mode to cold-mode accretion. In isolated galaxies at this mass scale, the virial temperature is sufficiently high ($T_{\text{vir}} \sim 10^6$ K) that radiative cooling operates on timescales longer than the dynamical time, allowing gas to remain near the virial temperature as it accretes. However, mergers disrupt this equilibrium through multiple physical mechanisms: tidal compression and shocks heat and compress infalling streams and CGM gas, temporarily raising densities while the post-shock cooling drives gas toward the thermally unstable regime where $t_{\text{cool}} \sim t_{\text{ff}}$. The subsequent fragmentation and condensation of this thermally unstable gas creates a multiphase medium with substantial cool, dense clumps embedded in the hot halo, as evidenced by the extended tail toward lower temperatures in the phase diagrams (Fig. 6). Once $t_{\text{cool}} < t_{\text{ff}}$ is established over significant halo volumes, gas rapidly loses thermal support and falls toward the galaxy before pressure forces can redistribute it, establishing a self-sustaining cold accretion mode. This transition explains both the enhanced cool gas inflows (Fig. 7) and the elevated star formation rates in merging systems.

3.5. Gas cycling in the CGM

To quantify the intensity of mass exchange between baryon reservoirs in and around the CGM, we introduce the CGM

gas cycling rate (t_{cycle}^{-1}):

$$t_{\text{cycle}}^{-1} \equiv \frac{\dot{M}}{M_{\text{CGM}}}, \quad (2)$$

where \dot{M} is the mass transfer rate and M_{CGM} is the total CGM mass. Its inverse, t_{cycle} , gives the characteristic gas cycling timescale or the characteristic time for a CGM-mass equivalent to be exchanged through a given pathway, so that t_{cycle}^{-1} expressed in Gyr^{-1} directly measures how rapidly the CGM turns over on cosmological timescales.

To evaluate pathway-specific t_{cycle}^{-1} , we track all halo baryons over matched time intervals (from companion galaxy entry into the halo to coalescence; identical elapsed time for isolated controls), dividing them into galaxy inflow/outflow, CGM, and large-scale inflow/outflow. Here “galaxy inflow” encompasses all gas entering the galaxy that subsequently joins the ISM or forms stars. The CGM and cosmic inflow are further split into cold/cool ($T < 10^5$ K) and warm/hot ($T \geq 10^5$ K) phases. We compute the mass transfer rate between each component pair at successive times and present the sample-averaged results as Sankey diagrams in Fig. 9.

Mergers drive a system-wide enhancement of multiphase gas cycling across the CGM, strengthening nearly all exchange pathways between cosmic inflow, CGM phases, galaxy inflow, and large-scale outflow. In isolated galaxies (Fig. 9c), cycling follows a quiescent, stratified pattern with low t_{cycle}^{-1} along most pathways: e.g., cold/cool CGM accretes onto the galaxy at only $\sim 0.04 \text{ Gyr}^{-1}$ ($t_{\text{cycle}} \sim 25$ Gyr, exceeding a Hubble time). In mergers (Fig. 9a), this rate doubles and other pathways show comparable or larger enhancements.

Most strikingly, compared with isolated galaxies, the effective transfer rate from cold/cool cosmic inflow to galaxy

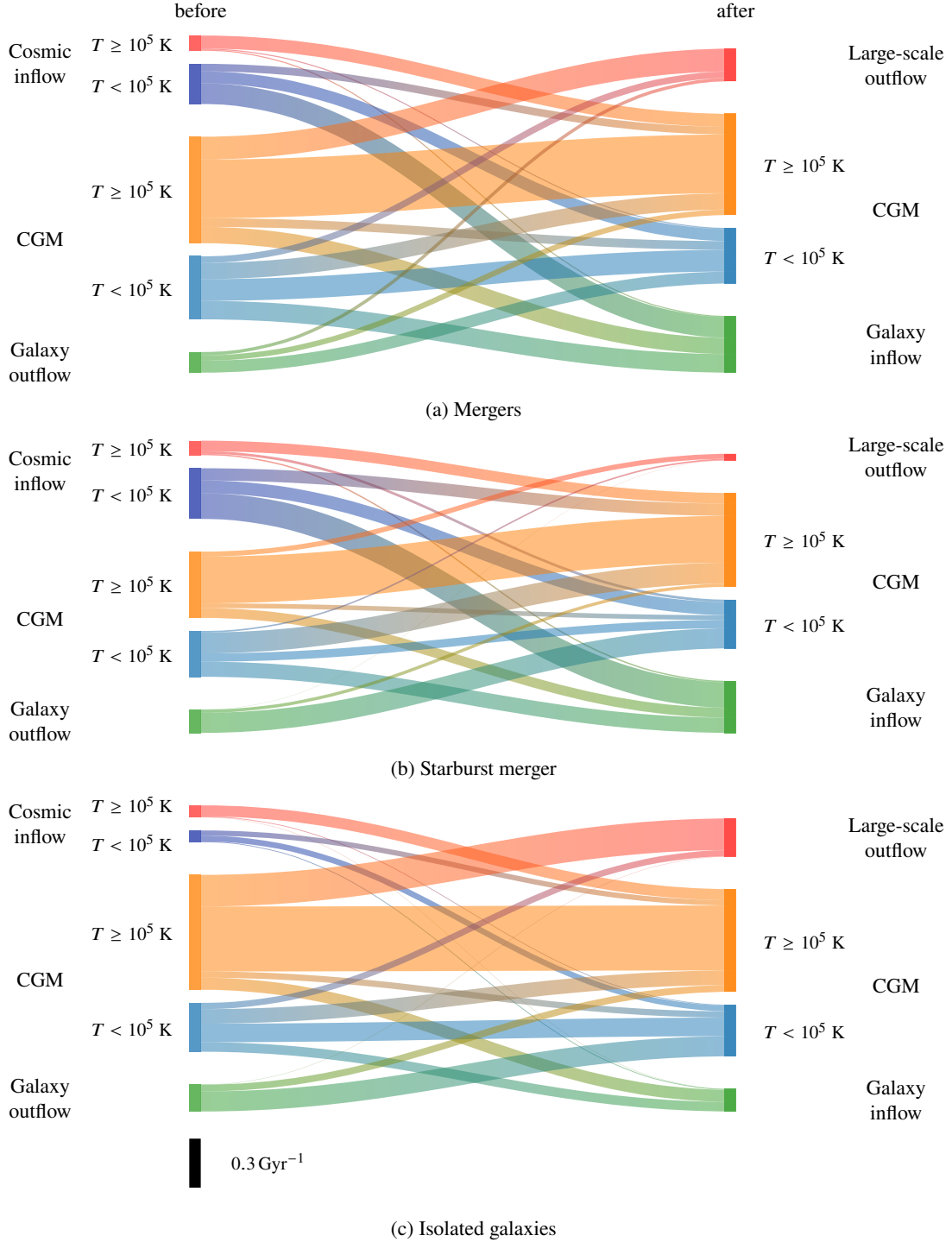


Figure 9. Sankey diagrams of the averaged CGM gas cycling rate t_{cycle}^{-1} (Eq. (2)) for (a) merging galaxies, (b) the starburst merger ($z = 0.11$ to $z = 0$), and (c) isolated galaxies. Left (right) nodes show the total t_{cycle}^{-1} from (into) each component at the earlier (later) redshift. Components: galaxy inflow (gas accreted into the ISM or forming stars), galaxy outflow, cold/cool CGM ($T < 10^5$ K), warm/hot CGM ($T \geq 10^5$ K), cold/cool and warm/hot cosmic inflow, and large-scale outflow. Flow widths scale with t_{cycle}^{-1} , and the absolute scale in Gyr^{-1} is shown in the bottom-left corner. Overall, merging systems exhibit enhanced t_{cycle}^{-1} across nearly all pathways, and the effective transfer rate from cold/cool cosmic inflow to galaxy inflow is amplified by factors of ~ 30 compared to isolated galaxies, reflecting rapid CGM processing and efficient fueling of the ISM.

inflow is amplified by factors of ~ 27 in mergers (Fig. 9a) and ~ 34 in the starburst merger (Fig. 9b), which corresponds to a dramatic reduction in the characteristic cycling timescale of the cold/cool cosmic gas from $t_{\text{cycle}} \sim 289$ Gyr in isolated systems to as short as ~ 11 Gyr in mergers and ~ 9 Gyr in the starburst merger. This dramatic enhancement does not necessarily imply direct ballistic accretion of cosmic gas penetrating the CGM into the ISM and stars; rather, it reflects rapid CGM processing: inflowing gas is efficiently cycled through intermediate CGM phases (cooling, condensing, and accreting) on timescales far shorter than in isolated halos. Merger-driven perturbations reduce CGM cooling times below free-fall times over large halo volumes (Fig. 8), effectively compressing the canonical inflow→CGM→ISM/stars sequence into a shortcut pathway in a time-averaged sense. Cosmic gas that would otherwise reside in the CGM for many Gyr is instead processed and delivered to the galaxy on timescales comparable to the merger duration.

Despite this acceleration, the CGM is not depleted: continuous replenishment from cosmic inflow and galaxy outflows sustains a comparable total CGM mass budget (as shown by Fig. 5), while cold/cool cosmic inflow becomes the dominant accretion channel, overtaking the warm/hot mode that prevails in isolated systems. The CGM in mergers is thus distinguished not by its mass but by its dynamics: it cycles gas far more rapidly, efficiently supplying fresh material to the ISM and fueling star formation on dynamical rather than cosmological timescales.

3.6. Ion column densities

We now examine the observational signatures of the enhanced multiphase CGM in merging galaxies by computing ion column densities along sightlines through the simulated halos. We select H I, Mg II, Si IV, N V, O VI, and Ne VIII which traces cold gas, $\approx 10^4$ K gas, $\approx 10^{4.9}$ K gas, $\approx 10^{5.2}$ K gas, $\approx 10^{5.5}$ K gas and $\approx 10^{5.8}$ K gas respectively. Fig. 10 presents the radial profiles of column density for the six key ions in both merging (red) and isolated (blue) systems, compared with available observational measurements.¹⁵ Following S. Ji et al. (2020), we use Trident (C. B. Hummels et al. 2017) to calculate these column densities. We use the UV background from C.-A. Faucher-Giguère et al. (2009) to predict the column density of H I, Mg II and Si IV and F. Haardt & P. Madau (2012) for N V, O VI and Ne VIII. The primary result is that merging galaxies exhibit statistically elevated column densities for low-ionization and intermediate-ionization species relative to isolated systems, while high-

ionization tracers show minimal differences between the two populations.

Merging systems display substantial enhancements in H I, Mg II, and Si IV column densities. H I shows an excess of factors ~ 10 – 100 in the inner to intermediate CGM ($0.2R_{\text{vir}} \lesssim r \lesssim 0.4R_{\text{vir}}$), declining to ~ 0.5 dex at larger radii. This result is similar to the observational work introduced in J. Wang et al. (2025), who utilize H I surface density images of 35 galaxies from FEASTS program and finds that in strongly tidal-interacting galaxy systems the H I profiles tend to deviate from other galaxies and become more flattened and thus have higher H I column density at outer region than other galaxies.

Similarly, Mg II exhibits an enhancement of approximately one order of magnitude at $R \sim 0.2R_{\text{vir}}$, increasing to larger factors beyond $0.4R_{\text{vir}}$. Si IV displays a comparable pattern, with mergers showing column densities exceeding those of isolated galaxies by more than one dex at $R > 0.2R_{\text{vir}}$. These enhancements reflect the increased cool gas content in merging systems demonstrated in Fig. 6, as these ions trace gas at temperatures $T \sim 10^4$ – 10^5 K. Compared with observational data, the simulated column densities for Mg II, Si IV, and N V in merging galaxies are not inconsistent with available measurements: the upper envelope of our simulated merger distributions traces the observed upper limits, though most observational constraints are upper or lower limits rather than detections, making definitive comparisons difficult. The simulated H I columns are slightly lower than observed values, but merging systems show better agreement than isolated galaxies. By excluding satellite galaxies, our sample may underestimate gas-rich satellite contributions to observed H I absorption.

Crucially, this excess in column density does not result from higher overall gas densities, as the total CGM gas density profiles are comparable between merging and isolated galaxies (shown in Fig. 5). Instead, the elevated ion columns arise directly from the altered thermal phase structure of the CGM: mergers substantially increase the mass fraction of cool gas (as shown in the extended tail toward lower temperatures in Fig. 6), thereby boosting the abundance of low- and intermediate-ionization species without significantly changing the total baryon content.

For intermediate-temperature ions, N V shows modest differences, with merging galaxies exhibiting relatively flat column density profiles between $0.1R_{\text{vir}}$ and $0.4R_{\text{vir}}$ while isolated systems decline steadily, resulting in an excess of $\gtrsim 0.5$ dex at $r \sim 0.4R_{\text{vir}}$. O VI, which traces gas near $T \sim 10^{5.5}$ K, displays even smaller differences: merging galaxies show only a $\lesssim 0.5$ dex enhancement at all radii compared to isolated systems. This modest excess is consistent with the relatively minor changes in warm gas content between the two populations. While simulated mergers exhibit higher

¹⁵ We note that while we analyze our simulations at $z = 0$, the observational samples span $0 < z < 0.4$ to ensure sufficient statistics, and narrowing to $z \approx 0$ would yield too few observations for meaningful comparison. Some discrepancies between simulations and observations may therefore arise from this redshift mismatch.

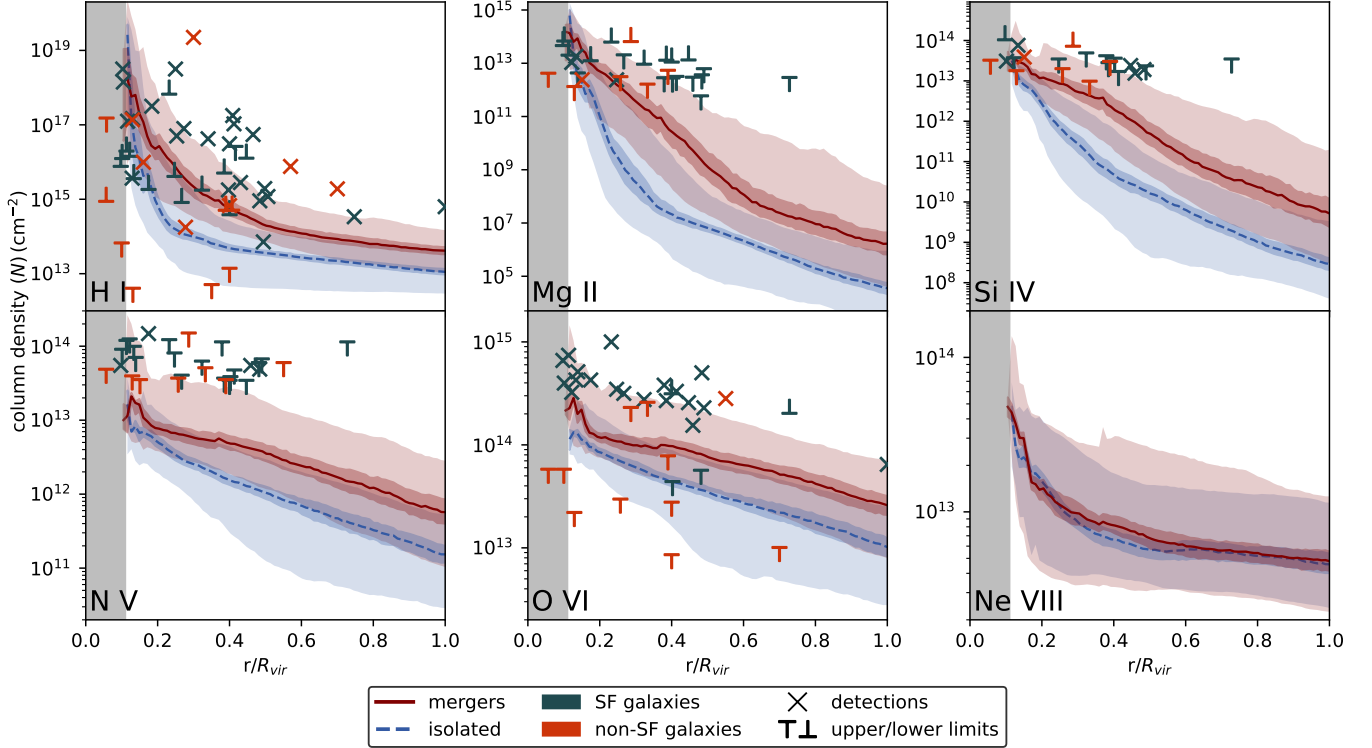


Figure 10. Radial profiles of ion column density for merging galaxies (red solid line) and isolated control galaxies (blue dashed line) as a function of galactocentric radius. Different panels show different ions, as labeled in the bottom left corner. Lines indicate median values, and inner darker shaded regions show the 16th to 84th percentiles of the median values via bootstrapping. Outer lighter region indicates the 16th to 84th percentiles of the category. Observational data from J. K. Werk et al. (2013); J. X. Prochaska et al. (2017a,b); S. D. Johnson et al. (2015); J. N. Burchett et al. (2019) are shown for comparison, with crosses representing detections and T symbols denoting upper/lower limits for star-forming (dark green) and non-star-forming (tangerine) galaxies. The observational samples are selected to match the stellar mass ($10^{10} < M_{\star} < 10^{11} M_{\odot}$) of our simulated galaxies.

O VI column densities than isolated galaxies, both populations appear somewhat underestimated compared to observations, with observational values typically lying near the upper envelope of our merger distribution and exceeding simulation medians by factors of ~ 2 . This discrepancy may reflect limitations in resolving turbulent mixing layers at a few 10 pc scales where O VI is efficiently produced (M. C. Begelman & A. C. Fabian 1990; S. Ji et al. 2019), the potential contribution of photoionized O VI supported by cosmic ray pressure (S. Ji et al. 2020), the lack of AGN feedback physics which may be able to enhance O VI column density (W. G. Mathews & J. X. Prochaska 2017; D. Nelson et al. 2018), or the exclusion of gas-rich satellites from our sample, none of which are fully captured in our simulations.

In contrast, Ne VIII, a tracer of hot gas ($T \gtrsim 10^6$ K), exhibits negligible differences between merging and isolated galaxies. Both populations display similar Ne VIII column densities declining from $N_{\text{Ne VIII}} \sim 5 \times 10^{13} \text{ cm}^{-2}$ at $r \sim 0.1 R_{\text{vir}}$ to $\sim 6 \times 10^{12} \text{ cm}^{-2}$ near R_{vir} . This lack of enhancement reflects the comparable hot gas fractions in both samples, as hot gas remains a minor component in both merging and isolated systems for the given halo mass range. Observation of Ne VIII is

not included in the figure due to the lack of Ne VIII observations within the mass range and redshift range ($0 < z < 0.4$), while as indicated in N. A. Wijers et al. (2024), FIRE-2 model have consistency with the observed Ne VIII column density in $\sim 10^{12} M_{\odot}$ halos but may under-predict its scatter.

4. DISCUSSION AND CONCLUSIONS

4.1. Discussion

We present a systematic comparison of circumgalactic medium (CGM) properties in merging versus isolated galaxies using the cosmological FIREbox simulation (R. Feldmann et al. 2023). By analyzing matched samples of 18 merging and 20 isolated systems with stellar masses $M_{\star} \sim 10^{10} - 10^{11} M_{\odot}$ at $z = 0$, we quantify how galaxy interactions fundamentally alter CGM thermodynamics, gas flows, and observational signatures.

Our results reveal how galaxy interactions reshape the circumgalactic medium and regulate baryon flows. Mergers alter the thermal structure of intermediate-mass halos by enabling efficient radiative cooling throughout significant portions of the CGM, overcoming the relatively long cooling times characteristic of isolated systems at similar masses. Gravitational

tional interactions introduce compressive motions, shocks, and mixing that reduce cooling times below free-fall times ($t_{\text{cool}} \lesssim t_{\text{ff}}$), producing the enhanced multiphase structure and elevated cool gas content we observe. In the context of mergers, the CGM emerges not as a passive reservoir but as a dynamically responsive system: merger-driven perturbations dramatically amplify both inflows and outflows by factors of ~ 10 – 100 across all temperature phases, particularly for the cool phase. This sensitivity implies that time-averaged models of CGM properties may systematically underestimate the true variability driven by interactions in realistic cosmological environments.

Our work emphasizes the critical role of the CGM as a rapidly cycling reservoir during mergers. Gas cycling analysis (Fig. 9) reveals that mergers enhance t_{cycle}^{-1} along nearly all pathways, most strikingly amplifying the effective transfer rate from cold/cool cosmic inflow to galaxy inflow by factors of ~ 27 – 34 , compared to isolated systems. This reflects rapid CGM processing: merger-driven perturbations compress the inflow→CGM→galaxy sequence by reducing cooling times below free-fall times, enabling inflowing gas to be cycled through CGM phases and accreted on dramatically shortened timescales, rather than cooling quiescently in the CGM as in isolated systems. Despite this acceleration, the total CGM mass remains comparable to isolated systems, underscoring the CGM’s role as a dynamic reservoir whose cycling rate — not mass — governs galaxy fueling during mergers. This cosmological context, including continuous baryon exchange while retaining material within the virial radius, has been emphasized in previous studies (B. P. Moster et al. 2011; M. H. Hani et al. 2018; M. Sparre et al. 2022) and cannot be captured by idealized merger simulations that lack ongoing environmental interactions.

The CGM transformation we identify has direct implications for star formation evolution during and after mergers. Our sample includes one merger-triggered starburst with specific star formation rates approximately half an order of magnitude above typical mergers, consistent with extensive observational evidence for merger-enhanced star formation (e.g., S. L. Ellison et al. 2008; D. R. Patton et al. 2013; Q. Huang et al. 2025). However, the CGM also plays a central role in galaxy quenching: post-merger galaxies are significantly more likely to shut down star formation than isolated systems (S. L. Ellison et al. 2022; W. Li et al. 2023). We suggest that both outcomes, including both starbursts and quenching, are linked to the same CGM processes operating at different merger phases. The enhanced radiative cooling and amplified inflows that fuel intense star formation during active merging can also be disrupted by powerful feedback or gas exhaustion in later merger stages, potentially contributing to subsequent quenching. While AGN feedback is often invoked as a quenching mechanism (P. F. Hopkins et al. 2008; A. Pontzen

et al. 2017; J. J. Davies et al. 2022; S. Wellons et al. 2023; L. Byrne et al. 2024), the detailed pathways remain debated (F. Rodríguez Montero et al. 2019; S. Quai et al. 2023), particularly for the intermediate-mass systems studied here.

Our simulations predict observational signatures that can be tested with CGM surveys. We find elevated ion column densities for low- and intermediate-ionization species in merging systems, reflecting the enhanced cool gas content. While simulated column densities are slightly lower than observed values, which is likely due to limited resolution of sub-kpc turbulent mixing layers (S. Ji et al. 2019; D. B. Fielding et al. 2020; B. Tan & S. P. Oh 2021), lack of AGN physics (W. G. Mathews & J. X. Prochaska 2017; D. Nelson et al. 2018) and exclusion of satellite galaxies, the predicted merger enhancement is consistent with available observational constraints. Observational validation faces two challenges: most CGM absorption surveys do not distinguish between isolated and merging galaxies, while many merger studies focus on galactic properties rather than the CGM (e.g., S. L. Ellison et al. 2008; D. R. Patton et al. 2013; X. Liu et al. 2011; G. Jin et al. 2021). Notable exceptions include R. Dutta et al. (2020) who found that galaxy groups exhibit significantly richer Mg II content and more complex kinematics than isolated galaxies, with similar enhancements reported by N. M. Nielsen et al. (2018) and Y.-H. Huang et al. (2021). Complementary 21 cm emission observations (T. Westmeier et al. 2022; J. Wang et al. 2023; X. Lin et al. 2025) can directly map neutral hydrogen distributions, with J. Wang et al. (2023) demonstrating that galaxy interactions trigger IGM cooling and generate diffuse H I, which is an in-situ gas generation mechanism via enhanced radiative cooling (X. Lin et al. 2025) consistent with our findings.

4.2. Conclusions

Our main conclusions are:

- *Mergers drive enhanced multiphase structure and amplified gas flows.* Merging systems display substantially broader distributions in temperature-density phase space, with pronounced enhancements in cool ($T \sim 10^4$ K), dense gas compared to isolated galaxies. Both inflow and outflow mass fluxes increase by at least 1 dex across all temperature phases, with cool gas net inflow enhanced by a factor of ~ 20 and warm gas by a factor of ~ 4 . This cool gas supply arises predominantly from in-situ radiative cooling within the CGM rather than from pre-existing cold streams. Notably, while the total baryon content within the virial radius remains comparable between merging and isolated systems, mergers fundamentally alter the phase distribution and the multiphase flow dynamics of CGM gas.

- *Mergers trigger enhanced radiative cooling in the CGM.* Merging galaxies exhibit cooling times shorter than free-fall times ($t_{\text{cool}} \lesssim t_{\text{ff}}$) throughout significant portions of their CGM. This condition, largely absent in isolated systems of comparable mass, indicates that mergers induce efficient radiative cooling. The resulting multiphase structure and enhanced cool gas content directly enable the amplified inflow rates described above, linking the cooling physics to the observed mass flux enhancements.
- *Mergers fundamentally accelerate CGM gas cycling.* The CGM gas cycling rate t_{cycle}^{-1} is enhanced along nearly all pathways in mergers. Most notably, the effective transfer rate from cold/cool cosmic inflow to galaxy inflow is amplified by factors of ~ 27 and ~ 34 in mergers and starburst mergers, respectively, corresponding to a reduction in the characteristic cycling timescale from $t_{\text{cycle}} \sim 289$ Gyr in isolated systems to ~ 11 Gyr in mergers and ~ 9 Gyr in the starburst merger. This reflects rapid CGM processing: inflowing gas is efficiently cycled through intermediate CGM phases on dramatically shortened timescales, rather than cooling quiescently in the CGM as in isolated systems. The CGM mass budget is maintained by replenishment from cosmic inflow and galaxy outflows; it is the cycling rate, not the reservoir mass, that distinguishes merging from isolated systems.
- *Mergers produce elevated low- and mid-ion column densities in the inner CGM.* The enhanced cool gas content in merging systems produces systematically elevated column densities for low- and intermediate-ionization species (H I, Mg II, Si IV, N V, O VI) in the inner to intermediate CGM, while high-ionization tracers like Ne VIII show negligible differences between populations.

4.3. Caveats

A few caveats should be kept in mind when interpreting our results.

Sample size: Our sample comprises 18 merging galaxies and 20 isolated control galaxies, which represents a relatively modest statistical sample. This limited size may not fully capture the full diversity of merger configurations (e.g., mass ratios, orbital parameters, merger stages) and their varied effects on CGM properties. Additionally, the inherent stochasticity in merger dynamics and CGM evolution means that larger samples are needed to robustly quantify systematic trends and reduce uncertainties. Future studies leveraging larger cosmological simulation volumes or extensive observational surveys would help validate and extend our findings across a broader parameter space.

Numerical resolution: We analyze the FIREbox simulation, where the adaptive spatial resolution varies with local gas density, with a baryonic mass resolution of $6.26 \times 10^4 M_{\odot}$. In the CGM, where typical hydrogen number density of warm/hot gas is around 10^{-4} cm^{-3} , this corresponds to an effective spatial resolution of ~ 10 kpc or less (C.-A. Faucher-Giguère & S. P. Oh 2023). While sufficient to capture large-scale CGM structures and flows, this resolution may not fully resolve small-scale thermal instabilities (M. McCourt et al. 2018), turbulent cascades, and mixing processes (S. Ji et al. 2019; M. Gronke et al. 2022) that operate on sub-kpc scales, thus potentially underestimating the efficiency of radiative cooling and the production of multiphase gas (C. B. Hummels et al. 2019). This may contribute to the systematically lower ion column densities (M. S. Peeples et al. 2019; F. van de Voort et al. 2019) we find compared to observations, particularly for low-ionization species that trace cool, dense gas produced by mixing layers. However, we must also emphasize that although the formation process of cold/cool gas may be under-resolved, the cold/cool, dense gas itself could be better resolved than warmer gas due to the meshless-finite-mass (MFM) method (P. F. Hopkins 2015) used in FIREbox simulations. Thus a higher resolution simulation will be valuable to further investigate the formation and evolution of cold/cool gas in the CGM and test our findings.

Non-thermal physics: The FIREbox simulation does not include magnetic fields or cosmic rays, both of which may significantly influence CGM properties. Magnetic fields can provide non-thermal pressure support, modify the growth rates of hydrodynamic instabilities (S. Ji et al. 2018; B. D. Wibking et al. 2025), and suppress thermal conduction (P. F. Hopkins et al. 2020), thereby altering the structure and survival of cool gas clouds. Cosmic rays, if dynamically important, can drive galactic winds more efficiently (P. F. Hopkins et al. 2021; M. Ruszkowski et al. 2017), increase the scale height of the CGM, and modify its thermal and ionization structure by providing additional pressure support and heating through streaming instabilities (E. G. Zweibel 2013; X.-N. Bai et al. 2019; M. Weber et al. 2025). These effects could produce a more diffuse and “fluffy” CGM, affecting the thermal and ionization state of the CGM, potentially increasing predicted column densities for certain ion species and improving agreement with observations, as shown explicitly in (I. S. Butsky & T. R. Quinn 2018; I. S. Butsky et al. 2020; S. Ji et al. 2020). The absence of these processes in our simulations should be considered when comparing with observational data.

AGN feedback: The FIREbox simulation does not incorporate AGN feedback, including jet-driven outflows and radiative heating from accretion disks. AGN feedback can strongly affect the evolution of host galaxies (L. C. Ho 2008; R. S. Somerville & R. Davé 2015; K.-Y. Su et al. 2021; H. Zhang et al. 2025), inject significant amounts of energy and momen-

tum into the CGM (A. C. Fabian 2012; T. M. Heckman & P. N. Best 2014; R. J. Wright et al. 2024), suppress gas cooling and inflow (A. Dekel et al. 2009; D. Nelson et al. 2015; B. Zhu et al. 2023), and dramatically alter the multiphase structure of the CGM (J. Suresh et al. 2015; E. Zinger et al. 2020; R. Y. Talbot et al. 2021). However, given that our sample galaxies have relatively modest stellar masses ($M_{\star} \sim 10^{10} - 10^{11} M_{\odot}$) and likely host correspondingly lower-mass black holes, AGN feedback may play a less significant role in these systems. Simulation studies of AGN feedback in dwarf galaxies suggest negligible impacts on CGM-scale properties (T. Su et al. 2025), though the effects remain uncertain for the intermediate mass range explored in this work. We note that the some other FIRE simulations include AGN feedback physics (e. g. P. F. Hopkins et al. 2023; S. Wellons et al. 2023; L. Byrne et al. 2024; S. B. Ponnada et al. 2025), which would enable future investigations of these effects in the context of galaxy mergers.

Despite these caveats, our study provides a novel and systematic analysis of how galaxy interactions reshape the CGM in a cosmological context. Our findings highlight the critical role of mergers in driving enhanced radiative cooling, multiphase structure, and rapid gas cycling in the CGM, with direct implications for galaxy evolution during these transformative events. Future work with larger samples, higher resolution, and additional physics will further refine our understanding of the complex interplay between galaxy interactions and their circumgalactic environments.

DATA AVAILABILITY STATEMENT

The data supporting the plots within this article are available on reasonable request to the corresponding author. A public version of the GIZMO code is available at [http://](http://www.tapir.caltech.edu/~phopkins/Site/GIZMO.html)

www.tapir.caltech.edu/~phopkins/Site/GIZMO.html. FIRE-2 simulations are publicly available (A. Wetzel et al. 2023) at <http://flatathub.flatironinstitute.org/fire>. Additional data, including initial conditions and derived data products, are available at <https://fire.northwestern.edu/data/>.

ACKNOWLEDGMENTS

Authors are supported by the NSF of China (grants 12192223, 12522301, 12133008, and 12361161601), the China Manned Space Program (grants CMS-CSST-2025-A08 and CMS-CSST-2025-A10), the National Key R&D Program of China No. 2023YFB3002502, and the National SKA Program of China (No. 2025SKA0130100). C.-A F.-G was supported by NSF through grants AST-2108230 and AST-2307327; by NASA through grants 80NSSC22K0809, 80NSSC22K1124 and 80NSSC24K1224; by STScI through grant JWST-AR-03252.001-A; and by BSF through grant#2024262. This work was performed in part at the Aspen Center for Physics, which is supported by National Science Foundation grant PHY-2210452. Numerical calculations were run on the CFFF platform of Fudan University, the supercomputing system in the Supercomputing Center of Wuhan University, and the High Performance Computing Resource in the Core Facility for Advanced Research Computing at Shanghai Astronomical Observatory.

Software: GIZMO (P. F. Hopkins 2015), Trident (C. B. Hummels et al. 2017), Cloudy (G. Ferland et al. 2017), Matplotlib (J. D. Hunter 2007), NumPy (C. R. Harris et al. 2020), SciPy (P. Virtanen et al. 2020), yt (M. J. Turk et al. 2010; M. Turk et al. 2025)

REFERENCES

- Anglés-Alcázar, D., Faucher-Giguère, C.-A., Kereš, D., et al. 2017, *MNRAS*, 470, 4698, doi: [10.1093/mnras/stx1517](https://doi.org/10.1093/mnras/stx1517)
- Bahcall, J. N., & Spitzer, Jr., L. 1969, *ApJL*, 156, L63, doi: [10.1086/180350](https://doi.org/10.1086/180350)
- Bai, X.-N., Ostriker, E. C., Plotnikov, I., & Stone, J. M. 2019, *ApJ*, 876, 60, doi: [10.3847/1538-4357/ab1648](https://doi.org/10.3847/1538-4357/ab1648)
- Bassini, L., Feldmann, R., Gensior, J., et al. 2023, *MNRAS*, 525, 5388, doi: [10.1093/mnras/stad2617](https://doi.org/10.1093/mnras/stad2617)
- Begelman, M. C., & Fabian, A. C. 1990, *MNRAS*, 244, 26P
- Blitz, L., & Robishaw, T. 2000, *ApJ*, 541, 675, doi: [10.1086/309457](https://doi.org/10.1086/309457)
- Burchett, J. N., Tripp, T. M., Prochaska, J. X., et al. 2019, *ApJL*, 877, L20, doi: [10.3847/2041-8213/ab1f7f](https://doi.org/10.3847/2041-8213/ab1f7f)
- Butsky, I. S., Fielding, D. B., Hayward, C. C., et al. 2020, *ApJ*, 903, 77, doi: [10.3847/1538-4357/abbad2](https://doi.org/10.3847/1538-4357/abbad2)
- Butsky, I. S., & Quinn, T. R. 2018, *ApJ*, 868, 108, doi: [10.3847/1538-4357/aaeac2](https://doi.org/10.3847/1538-4357/aaeac2)
- Byrne, L., Faucher-Giguère, C.-A., Wellons, S., et al. 2024, *ApJ*, 973, 149, doi: [10.3847/1538-4357/ad67ca](https://doi.org/10.3847/1538-4357/ad67ca)
- Davies, J. J., Pontzen, A., & Crain, R. A. 2022, *Monthly Notices of the Royal Astronomical Society*, 515, 1430, doi: [10.1093/mnras/stac1742](https://doi.org/10.1093/mnras/stac1742)
- Dekel, A., Birnboim, Y., Engel, G., et al. 2009, *Nature*, 457, 451, doi: [10.1038/nature07648](https://doi.org/10.1038/nature07648)
- Deng, Y., Li, H., Marinacci, F., et al. 2025, *A&A*, 704, A240, doi: [10.1051/0004-6361/202556854](https://doi.org/10.1051/0004-6361/202556854)
- Donahue, M., & Voit, G. M. 2022, *PhR*, 973, 1, doi: [10.1016/j.physrep.2022.04.005](https://doi.org/10.1016/j.physrep.2022.04.005)
- Dutta, R., Fumagalli, M., Fossati, M., et al. 2020, *MNRAS*, 499, 5022, doi: [10.1093/mnras/staa3147](https://doi.org/10.1093/mnras/staa3147)

- Ellison, S. L., Patton, D. R., Mendel, J. T., & Scudder, J. M. 2011, *MNRAS*, 418, 2043, doi: [10.1111/j.1365-2966.2011.19624.x](https://doi.org/10.1111/j.1365-2966.2011.19624.x)
- Ellison, S. L., Patton, D. R., Simard, L., & McConnachie, A. W. 2008, *AJ*, 135, 1877, doi: [10.1088/0004-6256/135/5/1877](https://doi.org/10.1088/0004-6256/135/5/1877)
- Ellison, S. L., Wilkinson, S., Woo, J., et al. 2022, *MNRAS*, 517, L92, doi: [10.1093/mnras/517/l92](https://doi.org/10.1093/mnras/517/l92)
- Fabian, A. C. 2012, *ARA&A*, 50, 455, doi: [10.1146/annurev-astro-081811-125521](https://doi.org/10.1146/annurev-astro-081811-125521)
- Faucher-Giguère, C.-A., Lidz, A., Zaldarriaga, M., & Hernquist, L. 2009, *ApJ*, 703, 1416, doi: [10.1088/0004-637X/703/2/1416](https://doi.org/10.1088/0004-637X/703/2/1416)
- Faucher-Giguère, C.-A., & Oh, S. P. 2023, *ARA&A*, 61, 131, doi: [10.1146/annurev-astro-052920-125203](https://doi.org/10.1146/annurev-astro-052920-125203)
- Feldmann, R., Hooper, D., & Gnedin, N. Y. 2013, *ApJ*, 763, 21, doi: [10.1088/0004-637X/763/1/21](https://doi.org/10.1088/0004-637X/763/1/21)
- Feldmann, R., Quataert, E., Faucher-Giguère, C.-A., et al. 2023, *MNRAS*, 522, 3831, doi: [10.1093/mnras/stad1205](https://doi.org/10.1093/mnras/stad1205)
- Ferland, G., Chatzikos, M., Guzmán, F., et al. 2017, *Revista mexicana de astronomía y astrofísica*, 53
- Fielding, D. B., Ostriker, E. C., Bryan, G. L., & Jermyn, A. S. 2020, *ApJL*, 894, L24, doi: [10.3847/2041-8213/ab8d2c](https://doi.org/10.3847/2041-8213/ab8d2c)
- Gill, S. P. D., Knebe, A., & Gibson, B. K. 2004, *MNRAS*, 351, 399, doi: [10.1111/j.1365-2966.2004.07786.x](https://doi.org/10.1111/j.1365-2966.2004.07786.x)
- Gronke, M., & Oh, S. P. 2018, *MNRAS*, 480, L111, doi: [10.1093/mnras/sly131](https://doi.org/10.1093/mnras/sly131)
- Gronke, M., & Oh, S. P. 2020, *MNRAS*, 492, 1970, doi: [10.1093/mnras/stz3332](https://doi.org/10.1093/mnras/stz3332)
- Gronke, M., Oh, S. P., Ji, S., & Norman, C. 2022, *MNRAS*, 511, 859, doi: [10.1093/mnras/stab3351](https://doi.org/10.1093/mnras/stab3351)
- Haardt, F., & Madau, P. 2012, *ApJ*, 746, 125, doi: [10.1088/0004-637X/746/2/125](https://doi.org/10.1088/0004-637X/746/2/125)
- Hafen, Z., Faucher-Giguère, C.-A., Anglés-Alcázar, D., et al. 2019, *MNRAS*, 488, 1248, doi: [10.1093/mnras/stz1773](https://doi.org/10.1093/mnras/stz1773)
- Hahn, O., & Abel, T. 2011, *MNRAS*, 415, 2101, doi: [10.1111/j.1365-2966.2011.18820.x](https://doi.org/10.1111/j.1365-2966.2011.18820.x)
- Hani, M. H., Gosain, H., Ellison, S. L., Patton, D. R., & Torrey, P. 2020, *MNRAS*, 493, 3716, doi: [10.1093/mnras/staa459](https://doi.org/10.1093/mnras/staa459)
- Hani, M. H., Sparre, M., Ellison, S. L., Torrey, P., & Vogelsberger, M. 2018, *MNRAS*, 475, 1160, doi: [10.1093/mnras/stx3252](https://doi.org/10.1093/mnras/stx3252)
- Harris, C. R., Millman, K. J., Van Der Walt, S. J., et al. 2020, *nature*, 585, 357
- Heckman, T. M., & Best, P. N. 2014, *ARA&A*, 52, 589, doi: [10.1146/annurev-astro-081913-035722](https://doi.org/10.1146/annurev-astro-081913-035722)
- Ho, L. C. 2008, *ARA&A*, 46, 475, doi: [10.1146/annurev.astro.45.051806.110546](https://doi.org/10.1146/annurev.astro.45.051806.110546)
- Hopkins, P. F. 2015, *MNRAS*, 450, 53, doi: [10.1093/mnras/stv195](https://doi.org/10.1093/mnras/stv195)
- Hopkins, P. F., Chan, T. K., Ji, S., et al. 2021, *MNRAS*, 501, 3640, doi: [10.1093/mnras/staa3690](https://doi.org/10.1093/mnras/staa3690)
- Hopkins, P. F., Hernquist, L., Cox, T. J., & Kereš, D. 2008, *ApJS*, 175, 356, doi: [10.1086/524362](https://doi.org/10.1086/524362)
- Hopkins, P. F., Wetzel, A., Kereš, D., et al. 2018, *MNRAS*, 480, 800, doi: [10.1093/mnras/sty1690](https://doi.org/10.1093/mnras/sty1690)
- Hopkins, P. F., Chan, T. K., Garrison-Kimmel, S., et al. 2020, *MNRAS*, 492, 3465, doi: [10.1093/mnras/stz3321](https://doi.org/10.1093/mnras/stz3321)
- Hopkins, P. F., Wetzel, A., Wheeler, C., et al. 2023, *MNRAS*, 519, 3154, doi: [10.1093/mnras/stac3489](https://doi.org/10.1093/mnras/stac3489)
- Huang, Q., Wang, J., Lin, X., et al. 2025, *ApJ*, 980, 157, doi: [10.3847/1538-4357/ad9579](https://doi.org/10.3847/1538-4357/ad9579)
- Huang, Y.-H., Chen, H.-W., Sheckman, S. A., et al. 2021, *MNRAS*, 502, 4743, doi: [10.1093/mnras/stab360](https://doi.org/10.1093/mnras/stab360)
- Hummels, C. B., Smith, B. D., & Silvia, D. W. 2017, *The Astrophysical Journal*, 847, 59
- Hummels, C. B., Smith, B. D., Hopkins, P. F., et al. 2019, *ApJ*, 882, 156, doi: [10.3847/1538-4357/ab378f](https://doi.org/10.3847/1538-4357/ab378f)
- Hunter, J. D. 2007, *Computing in science & engineering*, 9, 90
- Ji, S., Kereš, D., Chan, T. K., et al. 2021, *MNRAS*, 505, 259, doi: [10.1093/mnras/stab1264](https://doi.org/10.1093/mnras/stab1264)
- Ji, S., Oh, S. P., & Masterson, P. 2019, *MNRAS*, 487, 737, doi: [10.1093/mnras/stz1248](https://doi.org/10.1093/mnras/stz1248)
- Ji, S., Oh, S. P., & McCourt, M. 2018, *MNRAS*, 476, 852, doi: [10.1093/mnras/sty293](https://doi.org/10.1093/mnras/sty293)
- Ji, S., Chan, T. K., Hummels, C. B., et al. 2020, *MNRAS*, 496, 4221, doi: [10.1093/mnras/staa1849](https://doi.org/10.1093/mnras/staa1849)
- Jin, G., Dai, Y. S., Pan, H.-A., et al. 2021, *ApJ*, 923, 6, doi: [10.3847/1538-4357/ac2901](https://doi.org/10.3847/1538-4357/ac2901)
- Johnson, S. D., Chen, H.-W., & Mulchaey, J. S. 2015, *MNRAS*, 449, 3263, doi: [10.1093/mnras/stv553](https://doi.org/10.1093/mnras/stv553)
- Knollmann, S. R., & Knebe, A. 2009, *ApJS*, 182, 608, doi: [10.1088/0067-0049/182/2/608](https://doi.org/10.1088/0067-0049/182/2/608)
- Li, W., Nair, P., Rowlands, K., et al. 2023, *MNRAS*, 523, 720, doi: [10.1093/mnras/stad1473](https://doi.org/10.1093/mnras/stad1473)
- Lin, X., Wang, J., Staveley-Smith, L., et al. 2025, *ApJ*, 982, 151, doi: [10.3847/1538-4357/adb718](https://doi.org/10.3847/1538-4357/adb718)
- Liu, X., Shen, Y., Strauss, M. A., & Hao, L. 2011, *ApJ*, 737, 101, doi: [10.1088/0004-637X/737/2/101](https://doi.org/10.1088/0004-637X/737/2/101)
- Mathews, W. G., & Prochaska, J. X. 2017, *ApJL*, 846, L24, doi: [10.3847/2041-8213/aa8861](https://doi.org/10.3847/2041-8213/aa8861)
- McCourt, M., Oh, S. P., O'Leary, R., & Madigan, A.-M. 2018, *MNRAS*, 473, 5407, doi: [10.1093/mnras/stx2687](https://doi.org/10.1093/mnras/stx2687)
- McCourt, M., Sharma, P., Quataert, E., & Parrish, I. J. 2012, *MNRAS*, 419, 3319, doi: [10.1111/j.1365-2966.2011.19972.x](https://doi.org/10.1111/j.1365-2966.2011.19972.x)
- Moreno, J., Torrey, P., Ellison, S. L., et al. 2015, *MNRAS*, 448, 1107, doi: [10.1093/mnras/stv094](https://doi.org/10.1093/mnras/stv094)
- Moreno, J., Torrey, P., Ellison, S. L., et al. 2019, *Monthly Notices of the Royal Astronomical Society*, 485, 1320
- Moreno, J., Torrey, P., Ellison, S. L., et al. 2021, *MNRAS*, 503, 3113, doi: [10.1093/mnras/staa2952](https://doi.org/10.1093/mnras/staa2952)
- Moster, B. P., Macciò, A. V., Somerville, R. S., Naab, T., & Cox, T. J. 2011, *MNRAS*, 415, 3750, doi: [10.1111/j.1365-2966.2011.18984.x](https://doi.org/10.1111/j.1365-2966.2011.18984.x)

- Münch, G., & Zirin, H. 1961, *ApJ*, 133, 11, doi: [10.1086/146999](https://doi.org/10.1086/146999)
- Muratov, A. L., Kereš, D., Faucher-Giguère, C.-A., et al. 2015, *MNRAS*, 454, 2691, doi: [10.1093/mnras/stv2126](https://doi.org/10.1093/mnras/stv2126)
- Nelson, D., Genel, S., Vogelsberger, M., et al. 2015, *MNRAS*, 448, 59, doi: [10.1093/mnras/stv017](https://doi.org/10.1093/mnras/stv017)
- Nelson, D., Kauffmann, G., Pillepich, A., et al. 2018, *MNRAS*, 477, 450, doi: [10.1093/mnras/sty656](https://doi.org/10.1093/mnras/sty656)
- Nelson, D., Sharma, P., Pillepich, A., et al. 2020, *MNRAS*, 498, 2391, doi: [10.1093/mnras/staa2419](https://doi.org/10.1093/mnras/staa2419)
- Nielsen, N. M., Kacprzak, G. G., Pointon, S. K., Churchill, C. W., & Murphy, M. T. 2018, *ApJ*, 869, 153, doi: [10.3847/1538-4357/aaedbd](https://doi.org/10.3847/1538-4357/aaedbd)
- Pandya, V., Fielding, D. B., Anglés-Alcázar, D., et al. 2021, *MNRAS*, 508, 2979, doi: [10.1093/mnras/stab2714](https://doi.org/10.1093/mnras/stab2714)
- Patton, D. R., Torrey, P., Ellison, S. L., Mendel, J. T., & Scudder, J. M. 2013, *MNRAS*, 433, L59, doi: [10.1093/mnrasl/slt058](https://doi.org/10.1093/mnrasl/slt058)
- Patton, D. R., Wilson, K. D., Metrow, C. J., et al. 2020, *Monthly Notices of the Royal Astronomical Society*, 494, 4969
- Peeples, M. S., Corlies, L., Tumlinson, J., et al. 2019, *ApJ*, 873, 129, doi: [10.3847/1538-4357/ab0654](https://doi.org/10.3847/1538-4357/ab0654)
- Planck Collaboration, Ade, P. A. R., Aghanim, N., et al. 2016, *A&A*, 594, A13, doi: [10.1051/0004-6361/201525830](https://doi.org/10.1051/0004-6361/201525830)
- Ponnada, S. B., Cochrane, R. K., Hopkins, P. F., et al. 2025, *ApJ*, 980, 135, doi: [10.3847/1538-4357/ada280](https://doi.org/10.3847/1538-4357/ada280)
- Pontzen, A., Tremmel, M., Roth, N., et al. 2017, *MNRAS*, 465, 547, doi: [10.1093/mnras/stw2627](https://doi.org/10.1093/mnras/stw2627)
- Prochaska, J. X., Werk, J. K., Worseck, G., et al. 2017a, *ApJ*, 837, 169, doi: [10.3847/1538-4357/aa6007](https://doi.org/10.3847/1538-4357/aa6007)
- Prochaska, J. X., Tejos, N., cwotta, et al. 2017b, *pyigm/pyigm*: Initial release for publications, v1.0 Zenodo, doi: [10.5281/zenodo.1045480](https://doi.org/10.5281/zenodo.1045480)
- Qu, Z., Chen, H.-W., Rudie, G. C., et al. 2022, *MNRAS*, 516, 4882, doi: [10.1093/mnras/stac2528](https://doi.org/10.1093/mnras/stac2528)
- Quai, S., Byrne-Mamahit, S., Ellison, S. L., Patton, D. R., & Hani, M. H. 2023, *MNRAS*, 519, 2119, doi: [10.1093/mnras/stac3713](https://doi.org/10.1093/mnras/stac3713)
- Rodríguez Montero, F., Davé, R., Wild, V., Anglés-Alcázar, D., & Narayanan, D. 2019, *MNRAS*, 490, 2139, doi: [10.1093/mnras/stz2580](https://doi.org/10.1093/mnras/stz2580)
- Ruszkowski, M., Yang, H.-Y. K., & Zweibel, E. 2017, *ApJ*, 834, 208, doi: [10.3847/1538-4357/834/2/208](https://doi.org/10.3847/1538-4357/834/2/208)
- Somerville, R. S., & Davé, R. 2015, *ARA&A*, 53, 51, doi: [10.1146/annurev-astro-082812-140951](https://doi.org/10.1146/annurev-astro-082812-140951)
- Sparre, M., Pfrommer, C., & Ehlert, K. 2020, *MNRAS*, 499, 4261, doi: [10.1093/mnras/staa3177](https://doi.org/10.1093/mnras/staa3177)
- Sparre, M., Whittingham, J., Damle, M., et al. 2022, *MNRAS*, 509, 2720, doi: [10.1093/mnras/stab3171](https://doi.org/10.1093/mnras/stab3171)
- Springel, V., White, S. D. M., Tormen, G., & Kauffmann, G. 2001, *MNRAS*, 328, 726, doi: [10.1046/j.1365-8711.2001.04912.x](https://doi.org/10.1046/j.1365-8711.2001.04912.x)
- Stern, J., Fielding, D., Faucher-Giguère, C.-A., & Quataert, E. 2020, *MNRAS*, 492, 6042, doi: [10.1093/mnras/staa198](https://doi.org/10.1093/mnras/staa198)
- Stern, J., Faucher-Giguère, C.-A., Fielding, D., et al. 2021, *ApJ*, 911, 88, doi: [10.3847/1538-4357/abd776](https://doi.org/10.3847/1538-4357/abd776)
- Su, K.-Y., Hopkins, P. F., Bryan, G. L., et al. 2021, *MNRAS*, 507, 175, doi: [10.1093/mnras/stab2021](https://doi.org/10.1093/mnras/stab2021)
- Su, T., Ji, S., Yuan, F., Xia, H., & Zou, Y. 2025, arXiv e-prints, arXiv:2510.20897, doi: [10.48550/arXiv.2510.20897](https://doi.org/10.48550/arXiv.2510.20897)
- Suresh, J., Bird, S., Vogelsberger, M., et al. 2015, *MNRAS*, 448, 895, doi: [10.1093/mnras/stu2762](https://doi.org/10.1093/mnras/stu2762)
- Talbot, R. Y., Bourne, M. A., & Sijacki, D. 2021, *MNRAS*, 504, 3619, doi: [10.1093/mnras/stab804](https://doi.org/10.1093/mnras/stab804)
- Tan, B., & Oh, S. P. 2021, *MNRAS*, 508, L37, doi: [10.1093/mnras/slab100](https://doi.org/10.1093/mnras/slab100)
- Tumlinson, J., Peebles, M. S., & Werk, J. K. 2017, *ARA&A*, 55, 389, doi: [10.1146/annurev-astro-091916-055240](https://doi.org/10.1146/annurev-astro-091916-055240)
- Turk, M., Goldbaum, N. J., ZuHone, J. A., et al. 2025, *Introducing yt 4.0: Analysis and Visualization of Volumetric Data*, Tech. rep., Manubot
- Turk, M. J., Smith, B. D., Oishi, J. S., et al. 2010, *The Astrophysical Journal Supplement Series*, 192, 9
- van de Voort, F., Bieri, R., Pakmor, R., et al. 2021, *MNRAS*, 501, 4888, doi: [10.1093/mnras/staa3938](https://doi.org/10.1093/mnras/staa3938)
- van de Voort, F., Springel, V., Mandelker, N., van den Bosch, F. C., & Pakmor, R. 2019, *MNRAS*, 482, L85, doi: [10.1093/mnras/sly190](https://doi.org/10.1093/mnras/sly190)
- Virtanen, P., Gommers, R., Oliphant, T. E., et al. 2020, *Nature methods*, 17, 261
- Voit, G. M., Meece, G., Li, Y., et al. 2017, *ApJ*, 845, 80, doi: [10.3847/1538-4357/aa7d04](https://doi.org/10.3847/1538-4357/aa7d04)
- Wang, J., Yang, D., Oh, S.-H., et al. 2023, *ApJ*, 944, 102, doi: [10.3847/1538-4357/acafe8](https://doi.org/10.3847/1538-4357/acafe8)
- Wang, J., Yang, D., Lin, X., et al. 2025, *ApJ*, 980, 25, doi: [10.3847/1538-4357/ada95a](https://doi.org/10.3847/1538-4357/ada95a)
- Weber, M., Thomas, T., Pfrommer, C., & Pakmor, R. 2025, *A&A*, 698, A125, doi: [10.1051/0004-6361/202553954](https://doi.org/10.1051/0004-6361/202553954)
- Wellons, S., Faucher-Giguère, C.-A., Hopkins, P. F., et al. 2023, *MNRAS*, 520, 5394, doi: [10.1093/mnras/stad511](https://doi.org/10.1093/mnras/stad511)
- Werk, J. K., Prochaska, J. X., Thom, C., et al. 2013, *ApJS*, 204, 17, doi: [10.1088/0067-0049/204/2/17](https://doi.org/10.1088/0067-0049/204/2/17)
- Westmeier, T., Deg, N., Spekkens, K., et al. 2022, *PASA*, 39, e058, doi: [10.1017/pasa.2022.50](https://doi.org/10.1017/pasa.2022.50)
- Wetzel, A., Hayward, C. C., Sanderson, R. E., et al. 2023, *The Astrophysical Journal Supplement Series*, 265, 44
- Wibking, B. D., Voit, G. M., & O'Shea, B. W. 2025, *MNRAS*, 544, 2577, doi: [10.1093/mnras/staf1801](https://doi.org/10.1093/mnras/staf1801)
- Wijers, N. A., Faucher-Giguère, C.-A., Stern, J., Byrne, L., & Sultan, I. 2024, *ApJ*, 973, 99, doi: [10.3847/1538-4357/ad63a0](https://doi.org/10.3847/1538-4357/ad63a0)
- Wright, R. J., Somerville, R. S., Lagos, C. d. P., et al. 2024, *MNRAS*, 532, 3417, doi: [10.1093/mnras/stae1688](https://doi.org/10.1093/mnras/stae1688)
- Zahedy, F. S., Chen, H.-W., Johnson, S. D., et al. 2019, *MNRAS*, 484, 2257, doi: [10.1093/mnras/sty3482](https://doi.org/10.1093/mnras/sty3482)

Zhang, H., Xia, H., Ji, S., et al. 2025, ApJ, 985, 178,
doi: [10.3847/1538-4357/adcaba](https://doi.org/10.3847/1538-4357/adcaba)

Zhu, B., Yuan, F., Ji, S., et al. 2023, MNRAS, 524, 5787,
doi: [10.1093/mnras/stad2055](https://doi.org/10.1093/mnras/stad2055)

Zhu, G., & Ménard, B. 2013, ApJ, 773, 16,
doi: [10.1088/0004-637X/773/1/16](https://doi.org/10.1088/0004-637X/773/1/16)

Zinger, E., Pillepich, A., Nelson, D., et al. 2020, MNRAS, 499,
768, doi: [10.1093/mnras/staa2607](https://doi.org/10.1093/mnras/staa2607)

Zweibel, E. G. 2013, Physics of Plasmas, 20, 055501,
doi: [10.1063/1.4807033](https://doi.org/10.1063/1.4807033)